JOURNAL OF CLIMATE

Slow Modes of Global Temperature Variability in Regions of Weak Radiative Feedbacks and their Impact on Climate Sensitivity Estimates

ROBERT C. J. WILLS*, KYLE C. ARMOUR, AND DAVID S. BATTISTI

Department of Atmospheric Sciences, University of Washington, Seattle, WA

CRISTIAN PROISTOSESCU

University of Illinois, Urbana-Champaign, IL

LUKE A. PARSONS

Duke University, Durham, NC

ABSTRACT

Acting as both signal and noise, internal climate variability confounds estimates of the climate response to forcing but offers an opportunity to examine the dynamics controlling Earth's energy budget. This study analyzes the impact of low-frequency internal variability on global-mean surface temperature (GMST) and top-of-atmosphere (TOA) radiation in pre-industrial control simulations from the Coupled Model Intercomparison Project phase 6 (CMIP6). The results show that the slow modes of variability with the largest impact on decadal GMST anomalies are focused in high-latitude ocean regions, where they have a minimal impact on global TOA radiation. When these regions warm, positive shortwave cloud and sea ice-albedo feedbacks largely cancel the negative feedback of outgoing longwave radiation, resulting in a weak net radiative feedback. As a consequence of the weak net radiative feedback, less energy is required to sustain these long-lived temperature anomalies. In contrast to these weakly radiating high-latitude modes, the El Niño-Southern Oscillation (ENSO) has a large impact on the global energy budget, such that it remains the dominant influence on global TOA radiation out to decadal and longer timescales, despite its primarily interannual timescale. These results suggest that on decadal and longer timescales, different processes control internal variability in GMST than control internal variability in global TOA radiation. In light of these results, the contribution of low-frequency internal variability and ENSO to uncertainty in estimates of climate sensitivity from historical GMST and TOA-radiative-imbalance anomalies is discussed.

1. Introduction

a. Earth's energy budget

Earth's energy budget forms the basis for understanding changes in global-mean surface temperature (GMST). Energetic constraints suggest that surface temperatures will warm until they give rise to a radiative response that opposes the radiative forcing from an increase in greenhouse gases. In the simple case where the global radiative response depends linearly on the GMST anomaly $\overline{T}(t)$ (e.g., Gregory et al. 2004), the global energy imbalance $\overline{N}(t)$ at the top-of-atmosphere (TOA) is given by the sum of a global-mean radiative forcing $\overline{F}(t)$ and the global-mean radiative response $\overline{R}(t) = \lambda \overline{T}(t)$ according to:

$$\overline{N}(t) = \overline{F}(t) + \lambda \overline{T}(t). \tag{1}$$

Here, overbars denote a global mean and λ is the global radiative response per degree of global surface temperature change, called the *global climate feedback* (Charney et al. 1979; Dessler 2013). The TOA radiative fluxes $\overline{F}(t)$, $\overline{R}(t)$, and $\overline{N}(t)$ are all defined to be positive for downward radiation anomalies.

The global climate feedback λ provides the basis for determining Earth's *equilibrium climate sensitivity* (ECS), the global-mean surface warming that would result from a doubling of atmospheric CO_2 (and associated radiative forcing $\overline{F}_{2xCO_2} \approx 4$ W m^{-2}) once the climate system has reached equilibrium (Charney et al. 1979):

$$\text{ECS} = -\frac{\overline{F}_{2xCO_2}}{\lambda_{eq}}. \tag{2}$$

Here, λ_{eq} is the global climate feedback at equilibrium.

This energy budget framework has been used to estimate ECS from observations (Otto et al. 2013; Lewis and Curry 2015; Forster 2016; Knutti et al. 2017; Sherwood et al. 2020). Observational estimates of climate

*Corresponding author address: Robert C. Jnglin Wills, Department of Atmospheric Sciences, University of Washington, Seattle, WA 98195.
E-mail: rcwills@uw.edu

sensitivity rely on diagnosing the global climate feedback λ_{obs} from observations, based on the observed change in GMST $\overline{T}_{\text{obs}}$ and the corresponding radiative response $\overline{R}_{\text{obs}} = \overline{N}_{\text{obs}} - \overline{F}_{\text{obs}}$:

$$\text{EffCS} = -\frac{\overline{F}_{2\text{xCO}_2}}{\lambda_{\text{obs}}} = \frac{\overline{F}_{2\text{xCO}_2}\overline{T}_{\text{obs}}}{\overline{F}_{\text{obs}} - \overline{N}_{\text{obs}}}. \tag{3}$$

For example, Otto et al. (2013) estimate the climate sensitivity based on decadal anomalies in GMST, radiative forcing ($\overline{F}$), and global ocean heat uptake (an estimate of $\overline{N}_{\text{obs}}$) relative to pre-industrial values.

Here, the effective climate sensitivity (EffCS) in observations can differ from ECS (i.e., $\lambda_{\text{obs}} \neq \lambda_{\text{eq}}$), because the radiative response to warming depends not only on GMST but also on the spatial pattern of warming, a consequence of different radiative feedbacks in different regions (e.g., Armour et al. 2013; Andrews et al. 2015; Zhou et al. 2017; Dong et al. 2019). Assuming a linear superposition of the radiative feedbacks from warming in different regions, the global climate feedback λ can be expressed as

$$\lambda = \overline{\lambda(\mathbf{r})T'(\mathbf{r})}, \tag{4}$$

where $T'(\mathbf{r}) \equiv T(\mathbf{r})/\overline{T}$ is the local surface warming normalized by the global-mean surface warming (i.e., the spatial pattern of warming). The dependence of the global radiative feedback on the warming pattern

$$\lambda(\mathbf{r}) \equiv \frac{\partial \overline{N}}{\partial T(\mathbf{r})} \tag{5}$$

quantifies the global-mean TOA radiative response to local warming $T(\mathbf{r})$.

In order to constrain $\lambda(\mathbf{r})$, some studies have taken a forward modeling approach, imposing warming in different regions and examining the global radiative response (Zhou et al. 2017; Dong et al. 2019). They find that the global radiative response can be reconstructed from the pattern of surface temperature anomalies using a Green's function approach. However, this Green's function depends on the climate model used and is difficult to validate with observations. It is also possible to constrain $\lambda(\mathbf{r})$ by simply regressing global TOA anomalies against local temperature. This has been used to examine the dependence of the global cloud radiative effect on local temperature in climate model simulations and observations (Zhou et al. 2017), but as these authors point out, it does not account for the correlations between temperature anomalies in different regions. Multiple linear regression can be used to account for the correlation between local surface temperature predictors of $\overline{N}$ in climate model output (Bloch-Johnson et al. 2020), but this problem becomes under-constrained when looking at the short observational record. An alternative approach is to use dimension reduction by determining a few relevant patterns of temperature variability (i.e., modes of variability) and examining their impact on $\overline{T}$ and $\overline{N}$. In the case where a forced climate change can be reconstructed as the sum of changes ΔX in all relevant climate modes (cf. fluctuation-dissipation theorem), the success of the Green's function approach used by Zhou et al. (2017) and Dong et al. (2019) suggests that the total global climate feedback can be determined by:

$$\lambda = \frac{\sum_X \left(\partial \overline{N}/\partial X\right) \Delta X}{\sum_X \left(\partial \overline{T}/\partial X\right) \Delta X}. \tag{6}$$

In this way, an analysis of the global temperature and radiative impacts of internal variability can give mechanistic insights into the global climate sensitivity in response to external forcing.

b. Internal variability in Earth's energy budget

Internal climate variability leads to unforced changes in GMST, ocean heat content, and TOA energy imbalance, such as is thought to have occurred during the so-called global-warming hiatus, from 1998-2013 (Meehl et al. 2011; Trenberth and Fasullo 2013; Kosaka and Xie 2013; England et al. 2014; Liu et al. 2016). Cold GMST anomalies are generally thought to result from a redistribution of energy within the climate system, such that more energy is contained within the deep ocean (Meehl et al. 2011; Chen and Tung 2014; Liu et al. 2016). However, unforced variability in TOA energy imbalance can also lead to unforced changes in GMST and the global energy budget (Brown et al. 2014; Xie et al. 2016; Proistosescu et al. 2018; Lutsko and Takahashi 2018). Internal variability can therefore lead to contributions to $\overline{T}_{\text{obs}}$ and $\overline{N}_{\text{obs}}$ that are not representative of the forced response, confounding estimates of the climate response to external forcing based on Eq. (3).

In order to consider the impact of internal variability on observational estimates of climate sensitivity, we split $\overline{T}_{\text{obs}}$ and $\overline{N}_{\text{obs}}$ into forced and internal components:

$$\text{EffCS} = \frac{\overline{F}_{2\text{xCO}_2}(\overline{T}_{\text{forced}} + \overline{T}_{\text{internal}})}{\overline{F} - \overline{N}_{\text{forced}} - \overline{N}_{\text{internal}}}. \tag{7}$$

As a motivating example, we take representative externally forced anomalies in GMST ($\overline{T}_{\text{forced}}$) and global TOA radiation ($\overline{N}_{\text{forced}}$) and superimpose internal variability in GMST ($\overline{T}_{\text{internal}}$) and global TOA radiation ($\overline{N}_{\text{internal}}$), as diagnosed from pre-industrial control simulations from the Coupled Model Intercomparison Project phase 6 (CMIP6, Eyring et al., 2016; see Section 2b for more detail on the simulations used). The spread in EffCS due to internal variability is computed as twice the standard deviation of 10-yr and 30-yr running-mean EffCS, respectively, using Eq. (7) (Figs. 1a and 1b).

The spread in EffCS depends on the amount of externally forced historical warming and the radiative response

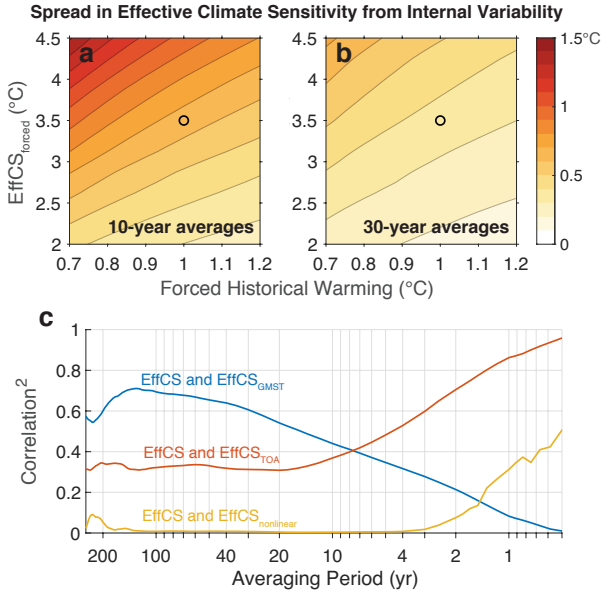

FIG. 1. Two-standard-deviation (≈95%) spread in effective climate sensitivity (EffCS) from superimposing internal variability from CMIP6 pre-industrial control runs on an assumed externally forced historical warming ($\overline{T}_{\text{forced}}$, x-axis) and a radiative response corresponding a forced effective climate sensitivity [$\text{EffCS}_{\text{forced}} = \left(\overline{F} - \overline{N}_{\text{forced}}\right)/\overline{T}_{\text{forced}}$, y-axis], with EffCS calculated from (a) 10-yr running averages and (b) 30-yr running averages of Eq. (7). Values are the median across 35 CMIP6 models. (c) Multi-model mean squared correlation between internal variability in EffCS and its components due to internal variability in GMST ($\overline{T}_{\text{internal}}$) and global TOA radiation ($\overline{N}_{\text{internal}}$), as a function of the averaging period used to compute EffCS. See Appendix A for more details of this decomposition.

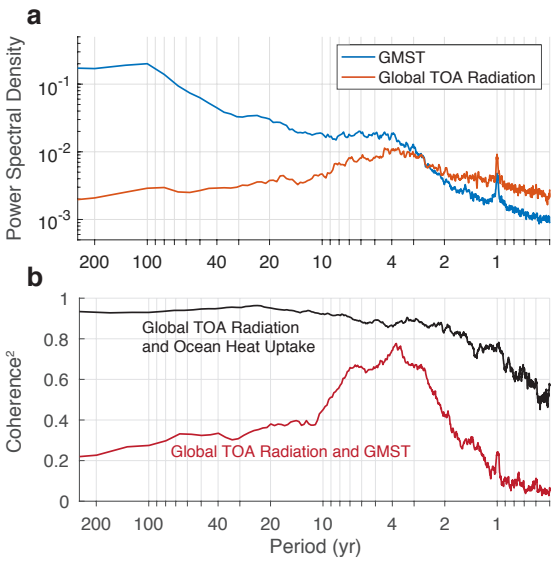

FIG. 2. (a) Power spectral density of GMST and global-mean TOA radiation. (b) Squared coherence between GMST and global-mean TOA radiation and between global-mean TOA radiation and the global-mean net surface heat flux (ocean heat uptake). All calculations are averaged over 35 CMIP6 piControl runs.

to that historical warming (quantified here with an effective climate sensitivity, $\text{EffCS}_{\text{forced}}$); the spread in EffCS is largest for a small historical warming or a weak global radiative response (higher $\text{EffCS}_{\text{forced}}$). For an externally forced historical warming $\overline{T}_{\text{forced}} = 1°\text{C}$ and radiative response $\overline{F} - \overline{N}_{\text{forced}} = -1.14$ W m^{-2} (corresponding to $\text{EffCS}_{\text{forced}} = 3.5°\text{C}$), the spread in EffCS due to internal variability would be ±0.65°C based on 10-yr averages (Fig. 1a) or ±0.36°C based on 30-yr averages (Fig. 1b). This is comparable to the range of EffCS across historical simulations from the 100-member MPI-ESM1.1 large ensemble (±0.95°C based on 10-yr averages, Dessler et al. 2018).

At decadal and longer timescales, internal variability primarily influences EffCS through its impact on GMST rather than through its influence on global TOA radiation (Fig. 1c; see Appendix A for a full decomposition of the contributions to spread in EffCS). The importance of GMST variability stems partly from its red power spectrum and thus large amplitude of variability at decadal and longer timescales (Fig. 2a). In contrast, global TOA variability has a relatively white power spectrum, with peak variance in the ENSO band.

The spread in EffCS due to internal variability (±0.65°C) is smaller than the observational uncertainty range of 1.2-3.9°C given in Otto et al. (2013), which includes observational uncertainty in GMST, radiative forcing, and ocean heat content anomalies relative to the pre-industrial state. However, internal variability could lead to a systematic bias if the chosen period is in a phase of internal variability that leads to a particular bias in EffCS (an effect that is neglected in Otto et al. 2013). For example, Sherwood et al. (2020) show that differences between the observed pattern of warming and the projected pattern of long-term warming lead to a bias toward lower EffCS in the historical period. This observed SST anomaly pattern is generally found to be consistent with model estimates of internal variability (Watanabe et al. 2020; Olonscheck et al. 2020). Furthermore, internal variability is the main reason why EffCS can be sensitive to the chosen averaging period, as discussed in Forster (2016) and Loeb et al. (2016). We therefore aim to understand how different modes of internal variability contribute to anomalies in EffCS.

c. Modes of variability in global climate

Modes of sea-surface temperature (SST) variability such as the Atlantic Multidecadal Oscillation (AMO), Pacific Decadal Oscillation (PDO), El-Niño–Southern Oscillation (ENSO), and Interdecadal Pacific Oscillation (IPO)

have all been argued to play leading roles in the decadal modulation of GMST, ocean heat content, and the TOA energy imbalance. However, there is no consensus on the relative importance of these different modes. Some studies emphasize the importance of processes in the eastern equatorial Pacific (Meehl et al. 2011, 2013; Kosaka and Xie 2013; Trenberth and Fasullo 2013; England et al. 2014; Risbey et al. 2014; Liu et al. 2016), while others emphasize processes in the North Atlantic (Zhang et al. 2007; Keenlyside et al. 2008; DelSole et al. 2011; Muller et al. 2013; Chen and Tung 2014; Tung et al. 2018; Stolpe et al. 2018; Li et al. 2020) or the Southern Ocean (Martin et al. 2013; Latif et al. 2013; Brown et al. 2015; Cabré et al. 2017). These different conclusions arise in part because different models emphasize processes in different regions (Brown et al. 2015; Parsons and Hakim 2019; Parsons et al. 2020) and in part because the relationships between local temperature, global temperature, and global TOA radiation depend on the timescale of variability (Brown et al. 2015; Lutsko and Takahashi 2018).

In this paper, we quantify the impact of modes of low-frequency (interdecadal) SST variability on GMST and TOA energy imbalance in coupled climate models. Traditional indices of low-frequency variability (e.g., PDO, AMO, etc.) are problematic for this analysis for a number of reasons. For example, they are not in general independent of each other. This by itself could be circumvented with multiple linear regression. However, traditional indices are also highly sensitive to subtleties of their definitions (Frankcombe et al. 2015; Stolpe et al. 2017) and have been shown to mix together a number of physically distinct processes that may have different impacts on global climate (Newman et al. 2016; Wills et al. 2019a,b). Principal component analysis provides a promising candidate for defining independent climate indices, but it also has the tendency to mix together processes that occur on different timescales and in different regions (Chen and Wallace 2016; Chen and Tung 2017; Wills et al. 2018). We therefore use low-frequency component analysis (LFCA, Wills et al. 2018) to identify modes of interdecadal variability. This method identifies linear combinations of principal components that isolate variability at decadal and longer timescales. Model-based estimates of the impact of different modes of interdecadal variability on GMST and global TOA radiation are used to understand how these modes influence EffCS. We also contrast the global climate impacts of interdecadal variability with those of interannual ENSO variability, because ENSO has a large impact on GMST and the global energy budget across a wide range of timescales.

This paper is organized as follows. We describe the CMIP6 output and methods used in Section 2. In Section 3, we describe the slow modes of internal variability in CMIP6 models and quantify their impacts on GMST and global TOA radiation. We also compare with the impacts of ENSO on decadal variability in GMST and global TOA radiation. In Section 4, we quantify the impact of modes of internal variability on estimates of climate sensitivity. In Section 5, we diagnose the local shortwave and longwave components of global TOA radiation variability and discuss the mechanisms governing the slow modes of climate variability. In Section 6, we present our conclusions and discuss the implications of our results. We discuss the future work needed to apply the model-based understanding derived here toward attributing observed changes in Earth's energy budget.

2. Methods and climate model output

a. Low-Frequency Component Analysis

Wills et al. (2018, hereafter W18) demonstrate a statistical methodology – low-frequency component analysis (LFCA) – to identify characteristic spatial anomaly patterns of low-frequency variability. LFCA is based on linear discriminant analysis, which has been used for a number of other applications within climate science (Déqué 1988; Schneider and Griffies 1999; Venzke et al. 1999; Schneider and Held 2001; DelSole 2001; Ting et al. 2009; DelSole et al. 2011; Wills et al. 2020). W18 shows that LFCA can separate the influences of global warming, PDO, and ENSO on Pacific SSTs based on differences in their spatial patterns and timescales. Subsequent papers (Wills et al. 2019a,b) have shown that LFCA isolates the processes controlling low-frequency variability from those that are important at higher frequencies, for example isolating the role of ocean circulation changes in AMO and PDO variability.

LFCA solves for low-frequency patterns (LFPs), which are the linear combinations of a chosen set of empirical orthogonal functions (EOFs) that maximize the ratio of low-frequency to total variance in their corresponding timeseries (low-frequency components, LFCs). Here, we define low-frequency variance as that which makes it through a 10-yr lowpass filter. In this way, patterns of interdecadal variability show up as the leading LFPs, and LFP-1 is the linear combination of the included EOFs with the highest possible ratio of interdecadal-to-intradecadal variance. LFPs and LFCs are normalized such that the LFP shows the anomaly pattern corresponding to a 1-standard-deviation anomaly in the corresponding LFC, which has unit variance. The LFCs are mutually uncorrelated, but there can be pattern correlation between the LFPs. The main parameter in this analysis is the number n of EOFs retained. W18 explores the sensitivity to n for short ($\sim$100 year) observational data sets, however we find that our results are insensitive to n for the long model simulations analyzed here.

By first solving for the EOFs of the unfiltered data, LFCA uses information about the spatiotemporal covariance of both low-frequency and high-frequency variabil-

ity (i.e., the leading LFC has the highest ratio of low-frequency to high-frequency variance, whereas the leading principal component of lowpass filtered data would have the highest total low-frequency variance). Patterns of interdecadal variability (such as ENSO) therefore show up as the trailing LFCs. In this way, LFCA provides a new basis for the variability contained within the n leading EOFs that is sorted by timescale. In this paper, we also discuss the interannual ENSO signal captured by the least-low-frequency component (LLFC). The LLFC is the n'th LFC (i.e., the linear combination of the included EOFs with the lowest possible ratio of interdecadal-to-intradecadal variance).

b. CMIP6 pre-industrial control output

We analyze output from pre-industrial control (piControl) simulations of 35 coupled climate models from CMIP6 (Eyring et al. 2016). External forcing from greenhouse gasses, aerosols, ozone, and solar variability is fixed at pre-industrial levels throughout the simulations. We use the last 400 years of monthly output from each model's piControl simulations such that we include a total of 14,000 years of unforced variability in our analysis. All model output is quadratically detrended and interpolated to a common 2° analysis grid. SSTs are computed from the surface temperature output by setting all monthly values below the freezing point of sea water to the freezing point and masking out land. This avoids interpolating from each model's irregular ocean grid. TOA radiation anomalies are computed from the outgoing longwave radiation and reflected shortwave radiation. Incoming shortwave is not included, because it does not vary in time in these simulations.

We compute anomalies with respect to each model's climatological seasonal cycle such that we ignore inter-model differences in climatology. We concatenate each model's SST anomaly matrix into one large anomaly matrix for the multi-model ensemble. LFCA is used to compute the leading low-frequency components of global SSTs across all 35 piControl runs. We retain $n = 65$ EOFs to capture 63% of the total SST variance. The 10-yr lowpass filter is applied to each model separately to avoid filtering over the discontinuities between models.

Like principal component analysis, LFCA can mix together processes occurring in different regions. This is especially true for patterns with similar eigenvalues (i.e., similar ratios of interdecadal-to-intradecadal variance). For LFPs with similar eigenvalues, we apply a secondary rotation of the resulting LFPs in order to spatially localize them (cf. Kaiser 1958). In this rotation, the pattern correlation between LFPs is computed in specified regions: the Atlantic (45°S-80°N), the North Pacific (20°N-70°N), and the Southern Ocean (35-80°S). The pattern correlations between a pair of LFPs within each region make up one element of a matrix, the eigenvectors of which give linear combination coefficients that define the new rotated patterns. This rotation is applied separately for sets of LFPs for which the low-frequency variance fraction is similar (LFPs 4-6 in our case). For example, the rotated LFP-4′ is a linear combination of the original LFPs 4-6, where primes denote a rotated pattern. No rotation is needed for LFPs 1-3, because these patterns have distinct ratios of low-frequency to total variance in our analysis.

3. Slow modes of SST variability and their impact on global climate

The first six LFPs of the CMIP6 ensemble are shown in Fig. 3. LFP-1 and LFP-2 both show low-frequency variability of SST in the high-latitude oceans, with LFP-1 focused in the North Atlantic and LFP-2 focused in the Southern Ocean. LFP-1 is similar to the AMO-like pattern found in the Atlantic-only analysis of Wills et al. (2019a), with a temporal correlation of 0.94, and is also highly coherent (0.89) with the traditional AMO index on decadal and longer timescales. LFP-2 is similar to the leading LFP of Southern Ocean SSTs, when analyzed separately (not shown). LFP-3 is similar to the PDO. In particular, it has a spatial pattern similar to the PDO in observations (Mantua et al. 1997), a high coherence (0.96) with the traditional PDO index (Mantua et al. 1997) on decadal and longer timescales, and a temporal correlation of 0.87 with the LFC-PDO index defined by LFCA of Pacific SSTs (Wills et al. 2019b). While these LFPs explain less of the total surface temperature variance than the leading EOFs (2.0%, 1.1%, and 2.1%, respectively, cf. 11%, 3.3%, and 2.6% for the leading EOFs), they explain more of the surface temperature variance on decadal and longer timescales (11%, 5.0%, and 7.0%, respectively, cf. 8.9%, 5.0%, and 2.8% for the leading EOFs). Note that the LFPs show the SST pattern associated with the corresponding LFCs at lag-0, and lead-lag regressions of SST anomalies onto the LFCs show time evolving SST patterns (Wills et al. 2019a,b).

The next three LFPs show secondary modes of low-frequency SST variability in the Southern Ocean, Pacific, and North Atlantic, respectively. Because they all have similar ratios of interdecadal-to-intradecadal variance, a secondary rotation was applied to localize them spatially (see Section 2b). LFP-4′ shows an SST anomaly dipole between the Weddell and Amundsen-Bellingshausen Seas, a mode of variability identified (in GFDL CM2.1) by Zhang et al. (2017). LFP-5′ shows warming of the North Pacific, with some extension into the tropical Pacific along the path of the Pacific Meridional Mode (Chiang and Vimont 2004). It resembles the Victoria Mode (Bond et al. 2003), which is similar to the SST signature of the North Pacific Gyre Oscillation (NPGO; DiLorenzo et al. 2008). It also shows an SST anomaly dipole in the subpolar North

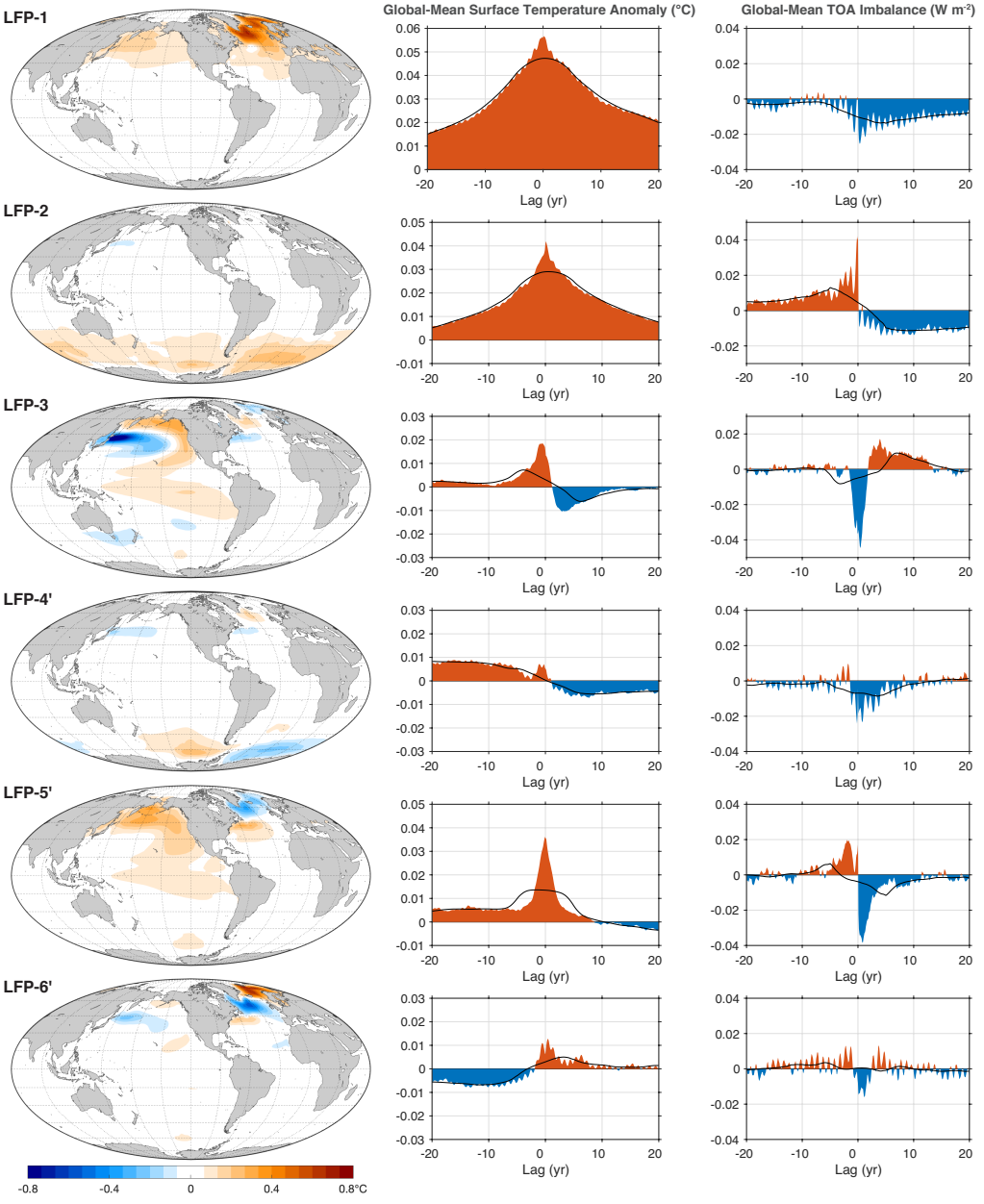

FIG. 3. Low-frequency patterns (LFPs) 1-6 of CMIP6 piControl runs and their impacts on global-mean surface temperature (GMST) and global-mean top-of-atmosphere (TOA) radiation. The left column shows the SST anomaly pattern (LFP). The middle column shows the lead-lag regression of monthly GMST anomalies on the associated low-frequency components (LFCs). The right column shows the lead-lag regression of monthly global-mean TOA radiation anomalies on the associated LFCs; negative values indicate a loss of energy to space. Black lines show the same lead-lag regressions, but for the 10-yr running means of GMST and global TOA radiation. Positive lags indicate anomalies that occur after the maximum anomaly in the LFC. All calculations are averaged over 35 CMIP6 models. A secondary rotation has been applied to LFPs 4-6 in order to localize them within ocean basins, as described in Section 2b.

Atlantic. By construction, its time evolution is orthogonal to the AMO-like LFC-1 and PDO-like LFC-3, at least in the multi-model mean. LFC-6′ is similar to the second LFP of the Atlantic-only analysis of Wills et al. (2019a), showing an SST anomaly in the subpolar gyre and opposite signed SST anomalies in the Gulf Stream, Greenland-Iceland-Norwegian (GIN) Seas, and Barents Sea, a well-known mode of Atlantic decadal variability (e.g., Menary et al. 2015). We find qualitatively similar patterns of low-

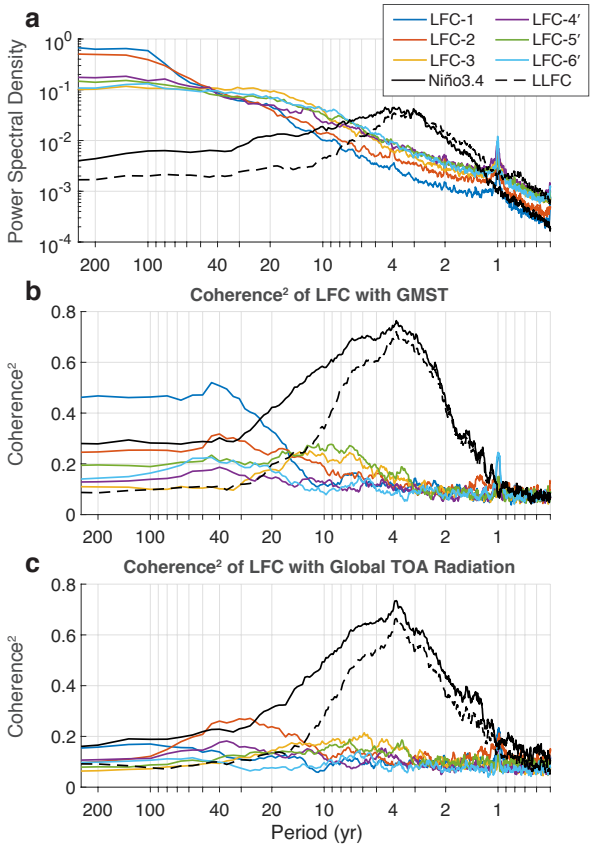

FIG. 4. (a) Power spectral density of low-frequency components (LFCs). (b) Squared coherence between the LFCs and GMST. (c) Squared coherence between the LFCs and global-mean TOA radiation. All panels also show Niño3.4 and least-low-frequency component (LLFC) for comparison. The LLFC is strongly correlated with Niño3.4 and is discussed in more detail in the text. All calculations are averaged over 35 CMIP6 piControl runs.

frequency internal variability in CMIP5 piControl simulations (not shown).

The first six LFPs all have red power spectra (Fig. 4a), with variance increasing out to multi-decadal and centennial timescales. While the multi-model mean power spectra do not show distinct spectral peaks at interannual and longer timescales, this does not rule out the possibility of spectral peaks in individual models. In this analysis of anomalies from the seasonal cycle, the annual peak in the power spectra arrises from the tendency of SST anomalies to reemerge each winter (Alexander et al. 1999).

a. Impacts on GMST

For each LFP, we compute the lead-lag regression of GMST anomalies onto the corresponding LFC (Fig. 3). The modes of high-latitude warming represented by LFP-1 and LFP-2 have large and long-lived impacts on GMST that are 0.056°C and 0.041°C per standard deviation at their maxima, respectively. The persistence of these patterns is such that a 1-standard-deviation anomaly in the respective indices is associated with a 0.047°C and 0.029°C anomaly in decadal running-mean GMST (black lines in Fig. 3). For reference, the standard deviation of monthly-mean (decadal-running-mean) GMST anomalies in the composite of the 35 CMIP6 piControl runs is 0.155°C (0.077°C). This means that these two modes of low-frequency variability explain ∼28% and ∼10% of the variability in decadal-running-mean GMST, respectively. The impact of these modes on GMST is also evident in their coherence with GMST out to centennial timescales (Fig. 4b).

The large impact of LFP-1 and LFP-2 on GMST evident in the multi-model composites (Fig. 3) results in part from the large amplitudes of these modes in a few models. LFP-1 is particularly active in EC-Earth3, CNRM-ESM2.1, CNRM-CM6.1, and IPSL-CM6A-LR (Figs. 5 and 6a), all models which use the Nucleus for European Modeling of the Ocean (NEMO) ocean model. LFP-2 is particularly active in BCC-CSM2-MR, GFDL-ESM4, IPSL-CM6A-LR, EC-Earth3, BCC-ESM1, and GFDL-CM4 (Figs. 5 and 6b), all models which use versions of either the Geophysical Fluid Dynamics Laboratory's Modular Ocean Model (MOM) or NEMO. These models are all among the CMIP6 models with the most interdecadal GMST variability (Parsons et al. 2020). However, even models that are not among these outliers show impacts of LFC-1 and LFC-2 on decadal GMST variability of ∼0.03°C and ∼0.018°C, respectively (Figs. 6a and 6b), and the same modes are found when these outlier models are excluded (not shown).

The impact of the PDO-like LFP-3 on GMST has a more complex temporal evolution, with its peak impact on GMST of 0.018°C occurring in the year before the LFC-3 maximum followed by a quick transition to a decade of anomalously cold temperatures (Fig. 3). The time evolution of its impact on GMST results from the time evolution in the SST pattern (Wills et al. 2019b). As a consequence of the opposite signed impacts at lead and lag times, the sign of LFC-3's impact on decadal-mean GMST is not robust across models (Fig. 6c). However, its impact on the rate of GMST change over the course of a decade is robustly negative (Fig. 6f). The large negative trend in GMST during LFP-3 events is consistent with other studies that have identified the PDO or IPO as playing a role in decades of reduced GMST rise (i.e., hiatus decades; Meehl et al. 2011; 2013; Kosaka and Xie 2013; Trenberth and Fasullo 2013; England et al. 2014; Liu et al. 2016; Middlemas and Clement 2016). This could partially result from the tendency of PDO events to follow El Niño events, which have a large impact on GMST (Jones 1989; Wigley 2000; Trenberth et al. 2002) and influence the North Pacific through the atmospheric bridge (Alexander et al. 2002). The coherence of LFC-3 and GMST

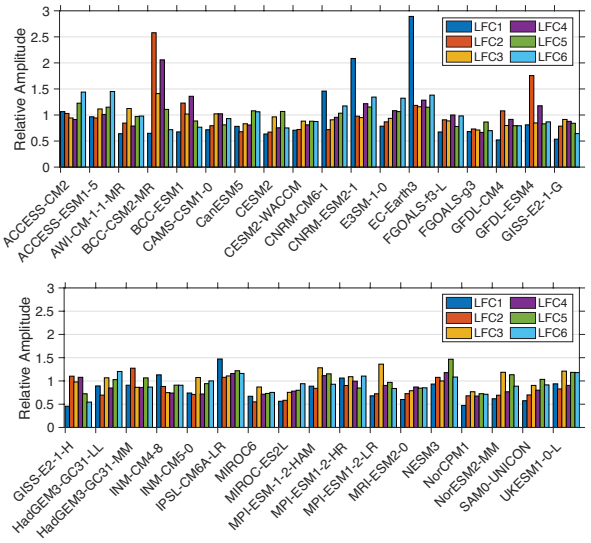

FIG. 5. Amplitude (standard deviation) of the six leading low-frequency components (LFCs) in each of the 35 CMIP6 piControl simulations, normalized by their amplitude in the multi-model composite.

is largest at 4-20 year timescales (Fig. 4b). The impact of LFC-5′ on GMST is actually somewhat larger in this same range of timescales (Fig. 4b). It has a peak impact on GMST of 0.036°C that occurs contemporaneously with the maximum in the SST pattern (i.e., at lag-0, Fig. 3). The amplitudes of these modes of Pacific decadal variability are relatively consistent across models (Fig. 5).

Due to their confinement to high latitudes and their cancelling positive and negative temperature anomalies in different regions, LFP-4′ and LFP-6′ have relatively small impacts on GMST (Fig. 3), even at multi-decadal timescales (Fig. 4b).

b. Impacts on global-mean TOA radiation

Internal variability in global-mean TOA radiation ($\overline{N}$) has much less power at decadal and longer timescales than does internal variability in GMST ($\overline{T}$); while 25% of internal $\overline{T}$ variability is on decadal and longer timescales, only 1% of internal $\overline{N}$ variability is (Fig. 2a). Variability in $\overline{N}$ is essentially white (i.e., its power spectral density does not vary with timescale) except for peaks in the ENSO band (3-5 years) and at annual timescales. The squared coherence between $\overline{T}$ and $\overline{N}$ is less than 0.4 at all timescale greater than a decade (Fig. 2b), suggesting that what TOA radiation variability there is at long timescales is stochastic and unpredictable. This also suggests that the mechanisms controlling GMST at decadal and longer timescales are not important for TOA radiation variability at these timescales. Variability in TOA radiation is highly coherent with variability in the net surface heat flux on decadal and longer timescales (Fig. 2b), such that the global-mean radiative flux at TOA is approximately the rate of global ocean heat uptake (cf. Palmer et al. 2011).

For each LFP, we compute the lead-lag regression of $\overline{N}$ anomalies onto the corresponding LFC (Fig. 3). Note that the time evolution of the TOA anomalies results in part from changes in the SST anomaly pattern over time. LFP-1 has a persistent TOA radiative impact of -0.011 W m^{-2} in the decade following its maximum (Table 1), indicating a loss of energy from the Earth system following the warm phase of LFP-1. These TOA radiative anomalies are small compared to the standard deviation of decadal-running-mean $\overline{N}$ anomalies (0.070 W m^{-2}), such that LFP-1 only accounts for 4% of the variance in $\overline{N}$ at decadal and longer timescales. The squared coherence between LFC-1 and $\overline{N}$ anomalies does not exceed 0.2 at any timescale (Fig. 4c). Thus, while LFP-1 is a major driver of decadal variability in global temperature, it has a minimal impact on the global TOA radiation.

The amplitude of global radiative anomalies associated with LFP-2 is similarly small (Fig. 3, Table 1). In addition to the weak but long-lived loss of energy after the warm phase of LFP-2, there is a net input of energy to the Earth system in the decades prior. This is evidence that LFP-2 is partially driven by TOA radiative anomalies. In Section 5, we discuss the particular radiative anomalies responsible, which point to a large role of the sea ice-albedo feedback in the multi-decadal variability of Southern Ocean temperature. LFC-2 has some coherence with $\overline{N}$ anomalies at 20-50 year timescales (Fig. 4c), but with TOA lagging by $\sim 90°$ (or, equivalently, $-$TOA leading by $\sim 90°$).

The warm phase of LFP-3 is associated with a short-lived negative global radiative response (energy out of the Earth system) followed by a persistent cooling of GMST and an associated positive global radiative response (energy into the Earth system, Fig. 3). Despite the shorter timescale of LFC-3 compared to LFC-1 and LFC-2, the associated anomalies in decadal running-mean $\overline{N}$ are nearly as large. LFP-5′ has a similar magnitude of impact on $\overline{N}$ to LFP-3, but with different time evolution. Like LFP-2, LFP-5′ appears to be amplified by global radiative feedbacks (i.e., during the evolution of a LFP-5′ warm event, TOA radiative fluxes are warming the surface at lead times and cooling the surface at lag times).

c. Impact of ENSO on global climate at decadal timescales

The dominant mode of interannual variability in the climate system is ENSO, which is often characterized by the Niño3.4 index (SST anomaly averaged over 5°S-5°N and 120-170°W). The broader SST anomaly pattern associated with Niño3.4, based on a regression of local SST anomalies on the Niño3.4 index, is shown in Fig. 7. In the models studied, Niño3.4 variance peaks at 3-5 yr timescales

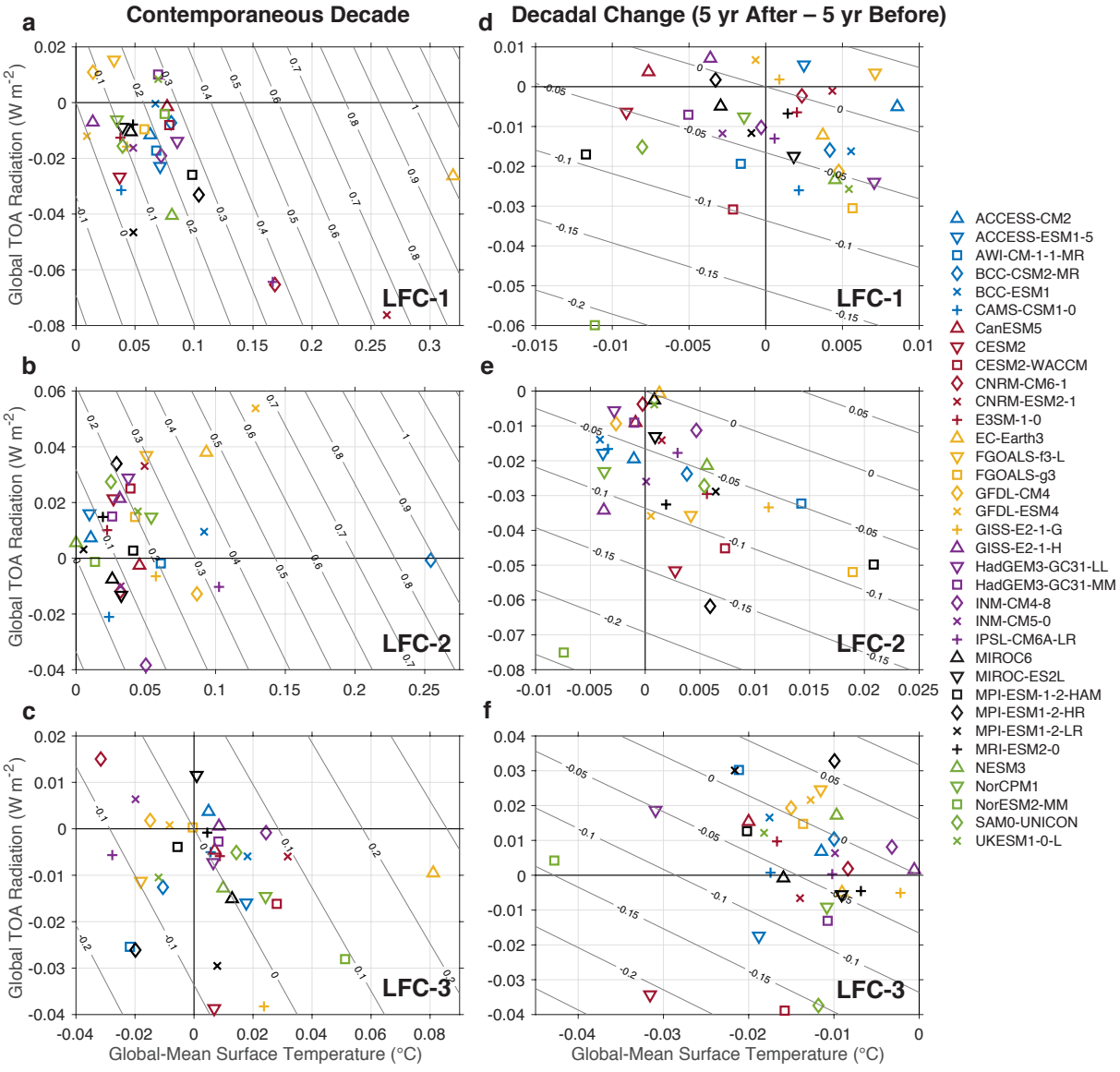

FIG. 6. Scatter plots of the lag-0 (contemporaneous) impact of a 2-standard-deviation anomaly in (a) LFC-1, (b) LFC-2, and (c) LFC-3 on 10-yr running-mean GMST (x-axis) and 10-yr running-mean global TOA radiation (y-axis) for all 35 of the CMIP6 piControl runs. (d)-(f) The change in GMST (x-axis) and global TOA radiation (y-axis) between the 5 years before and 5 years after a 1-standard-deviation anomaly in (d) LFC-1, (e) LFC-2, and (f) LFC-3. Diagonal lines show the corresponding anomaly in effective climate sensitivity (EffCS) if the these GMST and global TOA radiation anomalies are superimposed on a forced change of 1°C and 1.14 W m^{-2} (corresponding to an EffCS of 3.5°C). See Section 4 for more details.

(Fig. 4a). Here, we are interested in characterizing its impact on global climate at decadal and longer timescales.

Because Niño3.4 can be correlated with the leading LFCs (e.g., it has a 12% correlation with the PDO-like LFC-3), we also consider the representation of ENSO within the LFCA. Although ENSO still has power at decadal and longer timescales (Fig. 4a), its large amplitude at interannual timescales gives it a low ratio of interdecadal-to-intradecadal variance. For this reason, in the LFCA, much of the ENSO-like variance is captured by the least-low-frequency component (LLFC; Fig. 7), which is the linear combination of the included EOFs with the minimum ratio of interdecadal-to-intradecadal variance. The correlation between the LLFC and Niño3.4 is 0.77. Their spatial patterns are similar in the equatorial Pacific (within ±10° of the equator; Fig. 7), but the LLFC does not include associated SST anomalies in the extratopical North and South Pacific and in the Indian Ocean. Like

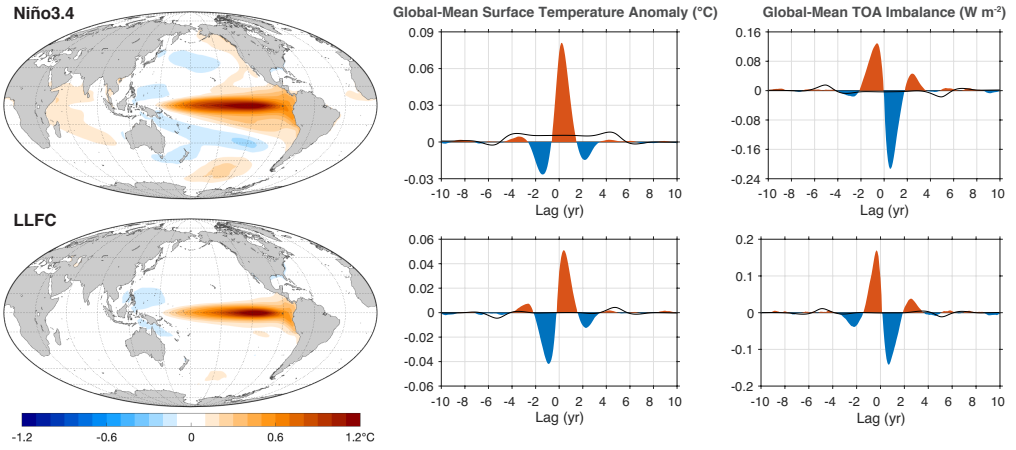

FIG. 7. ENSO and its impacts on global-mean temperature and global-mean TOA radiation, as characterized by Niño3.4 (top) and the least low-frequency component (LLFC, bottom). The left column shows the SST anomaly pattern per standard deviation in the associated index. The middle column shows the lead-lag regression of monthly GMST anomalies on the associated normalized ENSO index. The right column shows the lead-lag regression of monthly global-mean TOA radiative anomalies on the associated normalized ENSO index. Black lines show the same lead-lag regressions, but for the 10-yr running means of GMST and global TOA radiation. Positive lags indicate anomalies that occur after the maximum anomaly in the ENSO index. All calculations are are averaged over 35 CMIP6 models.

Niño3.4, the LLFC has its peak amplitude at 3-4 year timescales; however, it has a factor of two less variability at decadal and longer timescales (Fig. 4a). This shows that the LLFC is isolating the high-frequency component of ENSO. The LFC with the next-highest correlation with the Niño3.4 index is LFC-60 (i.e., the fifth LLFC), with a correlation of 0.32. LFC-60 shows warming in the central equatorial Pacific, cooling in the Kuroshio-Oyashio extension, and a positive anomaly in the Indian Ocean Dipole (IOD) (not shown); it is associated with Central Pacific El Niño events (Takahashi et al. 2011; Capotondi et al. 2015; Timmermann et al. 2018). Together these two LLFCs account for 69% of variance in Niño3.4.

ENSO, as captured by Niño3.4, has a large impact on GMST, which is well known (Jones 1989; Wigley 2000; Trenberth et al. 2002). In the CMIP6 models, the maximum GMST anomaly of 0.08°C per standard deviation occurs 2-3 months after the maximum Niño3.4 anomaly (Fig. 7). There are also weaker negative GMST anomalies at $\pm \sim 2$ yr, which are associated with the structure of the ENSO autocorrelation, because there is a tendency for La Niña years to follow El Niño years. The positive GMST anomaly associated with the LLFC is notably muted compared to that associated with Niño3.4; it peaks at 0.05°C per standard deviation at a lag of 5-6 months (Fig. 7). The LLFC leads Niño3.4 by 1-2 months, which explains the greater GMST lag. The coherence with GMST as a function of timescale is markedly different between Niño3.4 and the LLFC (Fig. 4b). While they have similarly large coherence with GMST in the ENSO band (2-5 yrs), the coherence between the LLFC and GMST drops off quickly at longer timescales, such that there is no significant coherence between the LLFC and GMST at 30-yr and longer timescales. In contrast, Niño3.4 still has a squared coherence of ∼30% with GMST at timescale ranging from multi-decadal to centennial. This analysis suggests that some of the impact of ENSO on GMST, especially that at decadal and longer timescales, comes from its teleconnections to regions outside the equatorial Pacific (which are not featured in the LLFC).

Interestingly, despite the relatively large squared coherence between Niño3.4 and anomalies in GMST at decadal and longer timescales (Fig. 4b), the maximum covariance between Niño3.4 and the 10-yr running-mean GMST anomaly (Fig. 7) only corresponds to a correlation of 0.1. This suggests that while ENSO has a substantial impact on GMST at decadal and longer timescales, its contributions cancel out between the different timescales that contribute to a decadal average (because of different phase relationships at different timescales), such that it has a small contribution to decadal-mean GMST anomalies in CMIP6 models.

The impact of ENSO on global TOA radiation is asymmetric about lag-0 (Fig. 7), meaning that the energy content of the Earth system is maximum near the peak of El Niño events, a result that has been confirmed in observations (Johnson and Birnbaum 2017). Peak energy input into the Earth system is 0.13 W m^{-2} per standard deviation 7 months before a Niño3.4 maxima and the peak energy loss is 0.21 W m^{-2} per standard deviation 6 months after a Niño3.4 maxima. The lead-lag covariance between global TOA radiation and ENSO is similar when quantified based on the LLFC, with modest changes in the peak radiative anomalies and a ∼2-month shift in the timing.

TABLE 1. Multi-model median statistics of decadal GMST ($\overline{T}$) and global TOA radiation ($\overline{N}$) variability. The stdev. column gives the total standard deviation of the each quantity. The LFC-1, LFC-2, LFC-3, LLFC, and Niño3.4 columns give the lag-5 covariance of the 10-yr running mean of the corresponding quantity with each of these indices (i.e., the anomaly in the decade following the maximum in each index, in units of the corresponding quantity per standard deviation). The global climate feedback is calculated as the 10-yr running-mean $\overline{N}$ anomaly divided by the 10-yr running-mean $\overline{T}$ anomaly. The lag-5 covariance is used because of inter-model differences in the sign of some $\overline{T}$ and $\overline{N}$ anomalies at lag-0 (cf. Figs. 6 and 8).

Mode	Stdev.	LFC-1	LFC-2	LFC-3	LLFC	Niño3.4
10-yr running-mean $\overline{T}$ (°C)	0.063	0.021	0.016	-0.005	0.003	0.005
10-yr running-mean $\overline{N}$ (W m^{-2})	0.064	-0.011	-0.009	0.004	-0.010	-0.017
Global Climate Feedback (W m^{-2} K^{-1})	-1.03	-0.50	-0.57	-0.70	-2.94	-3.20

Niño3.4 and the LLFC explain a similarly large fraction of global TOA radiation variance in the ENSO band (3-5 yrs), but the LLFC explains significantly less at longer timescales (Fig. 4c).

While the LLFC captures many of the same features of ENSO's impact on global climate as Niño3.4, it removes most of its variance and associated impacts on decadal and longer timescales. The LLFC removes some of the asymmetry between El Niño and La Niña events (not shown), and it may therefore underestimate the influence of extreme El Niños. The LLFC might serve as a useful ENSO index for some applications, but we use the more widely used Niño3.4 index for the analysis in the following sections.

d. Comparison of global climate feedbacks

We have shown that the leading modes of low-frequency variability have a large impact on GMST but a small impact on global TOA radiation (Fig. 3). To quantify the global radiative feedback associated with these modes and compare with the global radiative feedback associated with ENSO, we focus on the global climate anomalies in the decade following the maximum in each index (i.e., the 5-yr lagged covariance between 10-yr running mean GMST or global TOA radiation and each index; Table 1). This avoids near zero decadal-mean GMST anomalies associated with the PDO and LLFC at lag-0 (Figs. 3 and 7). The ratio of the global TOA radiation anomaly and the GMST anomaly gives the global climate feedback (Table 1). Global TOA radiation anomalies are defined as negative for energy loss from the Earth system, by convention, such that negative values of the global climate feedback quantify the strength of the negative (damping) feedback. The global climate feedbacks for LFC-1 and LFC-2 are small: -0.50 and -0.57 W m^{-2} K^{-1}, respectively. For comparison, the global climate feedback associated with an ECS of 3.5°C is approximately -1.1 W m^{-2} K^{-1}. If the global climate feedback was -0.5 W m^{-2} K^{-1} for a warming in response to greenhouse gas emissions, this would correspond to an ECS of 8°C (cf. Eq. 2). The global climate feedback associated with the cooling following a warm phase of LFC-3 is only slightly stronger: -0.70 W m^{-2} K^{-1}.

In contrast, ENSO has a small impact on decadal-mean GMST but a large impact on decadal-mean global TOA radiation (Table 1). This results in a large global climate feedback associated with the decay phase of ENSO: -2.94 or -3.20 W m^{-2} K^{-1} when quantified by the LLFC or Niño3.4, respectively. Radiative feedbacks this large for a warming in response to greenhouse gas emissions would correspond to an ECS of 1.25°C. In the next section, we consider how the contrasting global radiative feedback strengths associated with the LFCs and ENSO lead to differences in their effects on estimates of climate sensitivity from short records.

4. Impact of low-frequency internal variability on effective climate sensitivity

We showed in the introduction that the internal variability in CMIP6 models could lead to a spread of ±0.65°C in EffCS within 10-yr periods when it is superimposed on a forced response of 1°C and radiative feedbacks on this forced response corresponding to an EffCS of 3.5°C (Fig. 1a). In this section, we diagnose how different modes of internal variability contribute to this total spread in EffCS.

The impact of LFCs 1-3 on EffCS can be calculated from Fig. 6a-c, which show the impacts of 2-standard-deviation anomalies in LFCs 1-3 on decadal-mean anomalies in GMST and global TOA radiation. The corresponding anomalies in EffCS are diagonal lines in this space of GMST and global TOA radiation. LFC-1 and LFC-2, which both have large impacts on GMST at lag-0 (Fig. 6a, b), have correspondingly large impacts on EffCS of 0.18°C (the same for both LFCs in the multi-model median). The more positive TOA anomalies associated with LFC-2 affords it a comparable impact on EffCS despite its smaller impact on GMST compared to LFC-1 (for example, compare MPI-ESM1-2-HR between Figs. 6a and 6b). Anomalies are small enough that the impact of negative anomalies in these modes is approximately the negative of these values, such that the total spreads in EffCS due to LFC-1 and LFC-2 are each ±0.18°C (cf. total spread of ±0.65°C). The models with the largest amplitude variability in these modes (EC-Earth3 for LFC-1 and BCC-

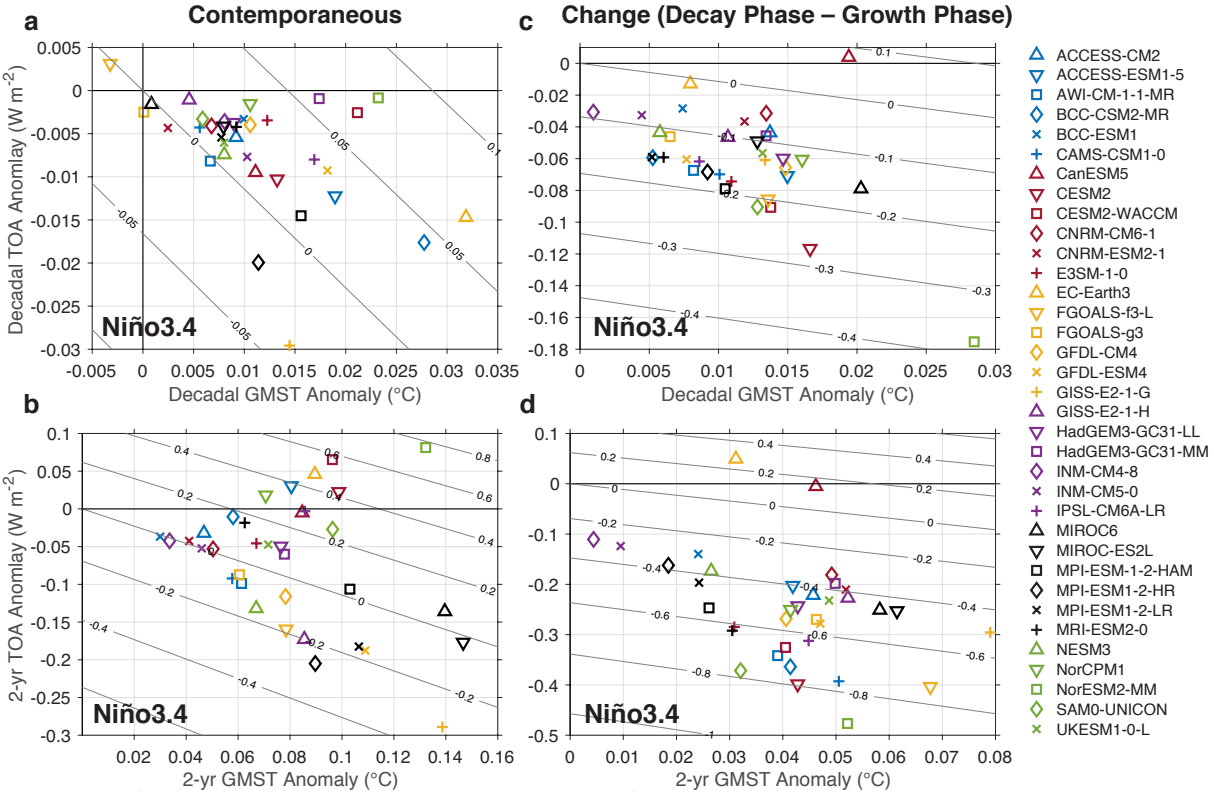

FIG. 8. (a) Scatter plots of the lag-0 (contemporaneous) impact of a 2-standard-deviation anomaly in Niño3.4 on 10-yr running-mean GMST (x-axis) and 10-yr running-mean global TOA radiation (y-axis) for all 35 of the CMIP6 piControl runs. (b) Same as (a), but for 2-yr running means. (c) The change in GMST (x-axis) and global TOA radiation (y-axis) between the 5 years before and 5 years after a 2-standard-deviation anomaly in Niño3.4. (d) Same as (c), but for 1-yr averages. Diagonal lines show the corresponding anomaly in effective climate sensitivity (EffCS) if the these GMST and global TOA radiation anomalies are superimposed on a forced change of 1°C and 1.14 W m^{-2} (corresponding to an EffCS of 3.5°C). See Section 4 for more details.

CSM2-MR for LFC-2) can have impacts on EffCS up to five times as large.

The lag-0 impact of the PDO-like LFC-3 on GMST is small and varies in sign across models (Fig. 6c), therefore contemporaneous (lag-0) LFC-3 anomalies have a minimal impact on EffCS. However, this does not capture the effect of GMST trends associated with LFC-3 (Fig. 3) on EffCS. We therefore analyze the change in GMST and global TOA radiation between the five years before and the five years after a 1-standard-deviation anomaly in an LFC (right hand side of Fig. 6). This captures decadal trends in GMST, global TOA radiation, and EffCS associated with each LFC. Qualitatively, this can also be thought of as the decadal global climate anomalies that would result from a positive LFC anomaly at the beginning of a decade and a negative anomaly at the end of a decade (i.e., the decadal anomalies associated with a 2 standard deviation trend in the LFC). Nearly all models show a reduction in the rate of global warming during positive PDO events (based on LFC-3, Fig. 6f), as has been suggested to explain the so-called global warming hiatus (Meehl et al. 2011; Trenberth and Fasullo 2013; Kosaka and Xie 2013; England et al. 2014; Liu et al. 2016). Equivalently, a negative trend in the PDO-like LFC-3 is associated with a negative GMST anomaly. Most models have a moderate radiative response to this cooling (with anomalous energy input into the Earth system), such that these anomalies do not have a big influence on EffCS (Fig. 6f). In a few models, including CESM2 and CESM2-WACCM, the radiative response is the opposite sign (a positive feedback). In this case, cooling trends associated with LFC-3 can induce moderate negative biases in EffCS.

LFC-1 and LFC-2 can similarly induce a negative EffCS bias in their decay phase in models where the global TOA radiation anomalies are highly asymmetric about lag-0 (Fig. 6d, e), such as NorESM2-MM. However, the decadal trends in GMST and EffCS associated with LFC-1 and LFC-2 are generally smaller than the contemporaneous anomalies in GMST and EffCS (Fig. 6a, b).

To investigate the influence of ENSO on decadal variability in EffCS, we examine a similar diagram based on the Niño3.4 index (Fig. 8). The lag-0 influence of Niño3.4 on decadal-mean GMST is small, leading to a small influence on EffCS (Fig. 8a). This is partly the result of cancellation between anomalies associated with El Niño and anomalies associated with La Niña, and the influence of Niño3.4 on 2-yr-mean GMST is more than five times larger (than on decadal-mean GMST) in the multi-model mean (Fig. 8b; cf. Fig. 8a). Because the lead-lag relationship between Niño3.4 and global TOA radiation is asymmetric about lag-0 (Fig. 7), the impact of Niño3.4 on decadal trends in global TOA radiation (i.e., the change between the five years before and the five years after) is much larger than its impact on the contemporaneous decade (Fig. 8c; cf. Fig. 8a; note the different y-scales). The trend in global TOA anomalies means that EffCS is much lower in the period following an El Niño or preceding a La Niña (when the Earth system is losing energy) than in the period preceding an El Niño or following a La Niña (when the Earth system is gaining energy). In this way, the timing of ENSO events within a decadal period can lead to biases in EffCS of ± 0.14°C (in the multi-model median). The end members of this 95% spread are decadal periods that begin at the peak of a 1-standard-deviation El Niño event and end at the peak of a 1-standard deviation La Niña event, or vice versa.

In summary, we find that the large impact of LFC-1 and LFC-2 on decadal GMST variability can lead to biases in EffCS based on decadal averages (Fig. 6a, b). The global climate impacts of modes of variability also differ between lead times and lag times, which can lead to time evolution of EffCS biases. The positive phases of LFCs 1-3 are associated with trends toward larger negative TOA radiation anomalies and thus trends toward more-negative biases in EffCS. This is particularly true for CMIP6 models that have the largest global TOA radiation change (toward more radiation out of the Earth system) between the five years before and the five years after a positive LFC anomaly (Fig. 6d-f). In fact, both the PDO (LFC-3) and ENSO (Niño3.4) influence EffCS primarily through their related trends in GMST and global TOA radiation (Figs. 6f and Figs. 8c); neither LFC-3 nor Niño3.4 have a robust influence on EffCS in the contemporaneous decade (Figs. 6c and Figs. 8a).

Part of the reason for the small influence of Niño3.4 on decadal-mean GMST and EffCS is the cancelling effects of ENSO variability on the different timescales that contribute to a decadal average, which is evident in the small correlation (0.1) of Niño3.4 with decadal running-mean GMST compared to the coherence between Niño3.4 and GMST on decadal and longer timescales (Fig. 4b). We hypothesize that a spectral treatment of the relationship between ENSO and global climate might better capture its influence on EffCS, but we leave this for examination in future work.

The complex phase relationships between modes of variability, GMST, and global TOA radiation mean that a detailed analysis of the contribution of modes of internal variability to EffCS biases in an individual decade would require a careful treatment of the phase evolution of modes of variability. In particular, we find that it is important to capture the full evolution of ENSO events within an averaging period, because EffCS will otherwise be strongly biased due to large differences in EffCS between the El Niño growth and decay phases.

5. Mechanisms of global radiative feedback

A key conclusion of our analysis thus far is that LFC-1 and LFC-2 have a weak global radiative feedback, such that their large impact on GMST on decadal and longer timescales does not translate into a large impact on global TOA radiation. In this section, we examine the particular global energy budget changes that lead to LFC-1 and LFC-2 having a weak global radiative feedback and compare to the global energy budget changes associated with LFC-3 and Niño3.4 variability. We focus on changes during the positive phases of these modes of variability, however, the linearity of our analysis implies that the same conclusions also apply, with opposite sign, to the negative phases of these modes of variability.

a. Atlantic Multidecadal Variability

The small global TOA radiation anomaly associated with LFC-1 (Atlantic multi-decadal variability; AMV) is the net result of large cancelling anomalies in the longwave (LW) and shortwave (SW) components (Fig. 9a). In the warm phase of the AMV, there is anomalous global energy loss resulting from a strengthening of outgoing longwave radiation (OLR). This negative feedback acts to damp the warm temperature anomalies. OLR anomalies are largest in the high-latitudes of the Northern Hemisphere (Fig. 9b; note that LW $= -$OLR), where surface air temperature anomalies are largest. There are also interesting spatial features such as the presence of positive LW anomalies in the Northern Hemisphere tropics and negative LW anomalies in the Southern Hemisphere tropics, indication of a northward shift of the Intertropical Convergence Zone (ITCZ) in response to warming of the high latitudes of the Northern Hemisphere (Chiang and Bitz 2005; Broccoli et al. 2006). The LW component alone would amount to a large global radiative feedback (-1.5 W m^{-2} K^{-1} based on decadal anomalies centered at lag-0). However, in the global mean, these LW anomalies are mostly cancelled by anomalies in SW.

SW anomalies are positive (net energy gain) in most regions of the globe (Fig. 9d). They are largest in the North Atlantic, where the SST anomalies are largest, but there

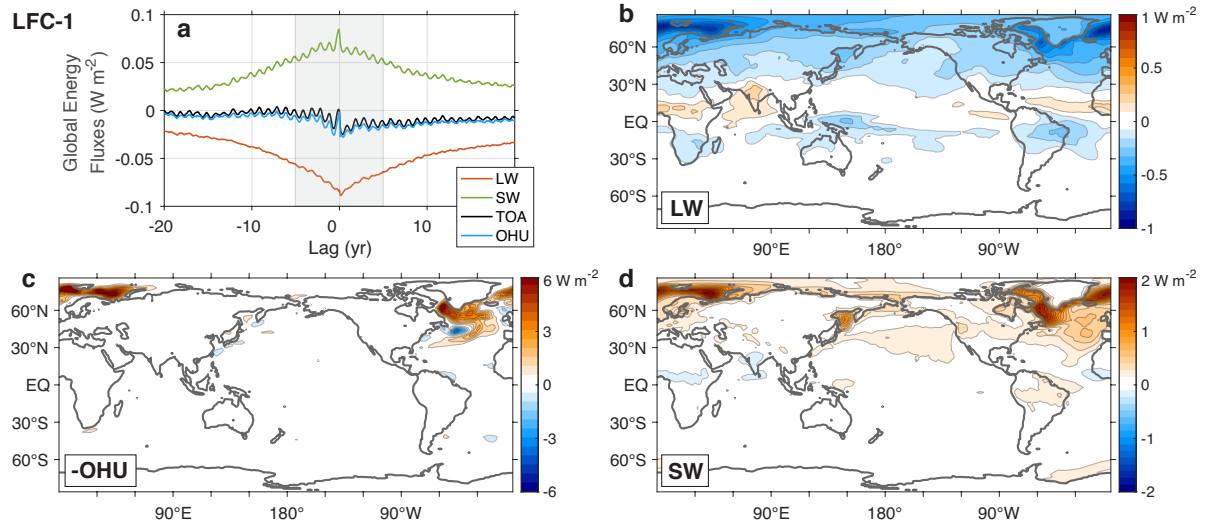

FIG. 9. Decadal-mean impact of LFC-1 (Atlantic multi-decadal variability) on the global energy budget. (a) Lead-lag regression of net incoming longwave radiation at TOA (LW), net incoming shortwave radiation at TOA (SW), net incoming radiation at TOA, and net ocean heat uptake (OHU) on LFC-1. Positive TOA flux anomalies correspond to a net energy input to the Earth system. Lag times indicate anomalies that lag LFC-1. (b)-(d) Maps of 10-yr running-mean anomalies in (b) LW, (c) −OHU, and (d) SW for a 1-standard-deviation anomaly in LFC-1. The gray shading in (a) shows the averaging period used in the other subpanels. All calculations are averaged over 35 CMIP6 models.

are also anomalies in the North Pacific. There are particularly large SW anomalies near the sea-ice edge, where warm SST anomalies lead to sea-ice loss and invoke a positive sea ice-albedo feedback. SW anomalies in the mid-latitude Northeast Atlantic are partially associated with a reduction in low-cloud cover, as evident in the reduction in reflected shortwave radiation. This supports the idea that cloud feedbacks act to amplify the AMV (Brown et al. 2016; Yuan et al. 2016; Bellomo et al. 2016). The positive cloud and sea ice-albedo feedbacks act to cancel the negative OLR feedback such that the net feedback is weakly negative (-0.22 W m^{-2} K^{-1} based on decadal anomalies centered at lag-0).

The net loss of energy at TOA comes almost entirely from the ocean, with little change in the energy stored in the global atmosphere (Fig. 9a). The ocean heat loss at the surface is concentrated in the subpolar North Atlantic (Fig. 9c), where the positive SSTs anomalies are largest (Fig. 3). This indicates the dominant role of ocean heat transport convergence anomalies (and thus the role of ocean circulations such as the Atlantic Meridional Overturning Circulation) in sustaining decadal SST anomalies in the North Atlantic (Wills et al. 2019a and references therein).

b. Southern Ocean Multidecadal Variability

The lead-lag regression of global TOA radiation on LFC-2 (Southern Ocean multi-decadal variability; SOMV) shows that the Earth system is gaining energy in the decades before and losing energy in the decades after the peak of a warm phase of the SOMV (Fig. 10a). However, the SW and LW components remain the same sign throughout the decades surrounding a SOMV event. The LW anomaly during an SOMV warm event is negative (a positive anomaly in OLR), and is concentrated in the high latitudes of the Southern Hemisphere (Fig. 10b), where surface air temperature anomalies are largest. The LW anomalies also show a hint of a southward ITCZ shift (positive anomalies in the Southern Hemisphere tropics and negative anomalies in the Northern Hemisphere tropics).

The global LW anomaly would strongly damp GMST anomalies associated with SOMV (-1.6 W m^{-2} K^{-1} based on decadal anomalies centered at lag-0) if it weren't for compensating anomalies in SW. These SW anomalies are concentrated in regions where sea ice is lost due to warming of the Southern Ocean (Fig. 10d), suggesting they are dominated by the sea ice-albedo feedback, although we find that cloud radiative changes also play a role in the positive shortwave feedback (not shown). As was the case for AMV, the shortwave feedbacks associated with SOMV act to cancel the negative OLR feedback such that the net feedback is weakly positive (0.16 W m^{-2} K^{-1} based on decadal anomalies centered at lag-0).

The global TOA radiation changes are balanced by changes in ocean heat content, with little contribution from atmospheric energy storage (Fig. 10a). The ocean heat loss and heat gain occur in different regions (Fig. 10c), with ocean heat loss occurring along the coast

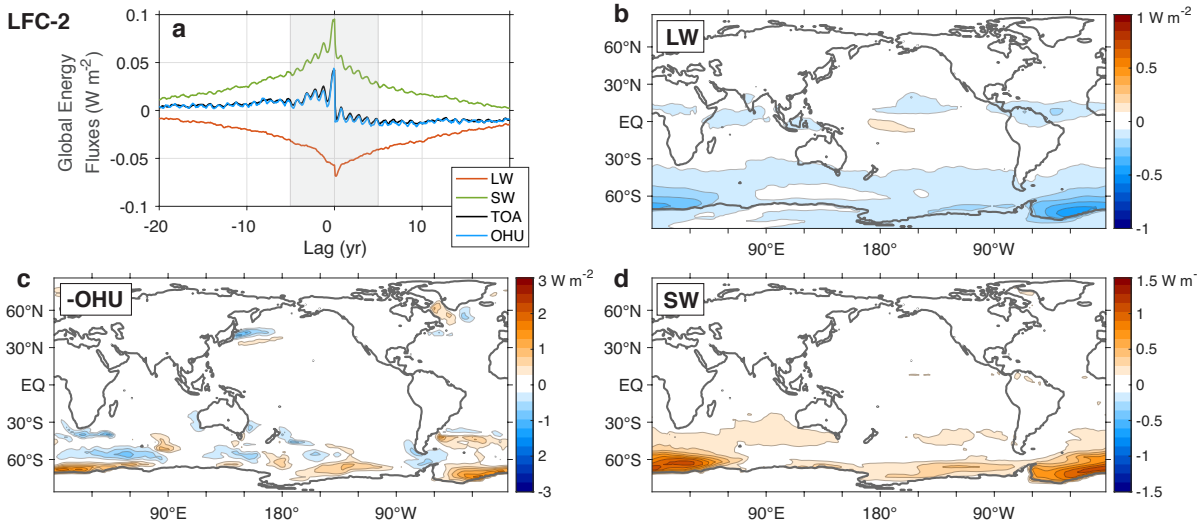

FIG. 10. Decadal-mean impact of LFC-2 (Southern Ocean multi-decadal variability) on the global energy budget. Panels as described in Fig. 9.

of Antartica and ocean heat uptake occurring further north, in the Indian and Pacific sectors of the Southern Ocean. The decadal ocean heat loss anomalies around Antarctica, in regions where SST anomalies are positive (Fig. 3), indicate a role of ocean heat transport convergence in sustaining these anomalies. Studies of models with large amplitude Southern Ocean multi-decadal variability (most of which use either the NEMO or MOM ocean models) have generally found this variability to be linked to open-ocean deep convection within polynyas (Martin et al. 2013; Pedro et al. 2016; Behrens et al. 2016; Reintges et al. 2017; Zhang et al. 2017; Cabré et al. 2017), which does not occur in all models. However, the presence of this variability in all of the CMIP6 models studied (albeit with a large spread in amplitudes and timescales), suggests that this mode of variability may be more general.

c. Pacific Decadal Oscillation

The lead-lag relationship of LW and SW anomalies with LFC-3 (Pacific Decadal Oscillation; PDO) is more complicated than for the first two LFCs (Fig. 11a). Global-mean LW anomalies are negative in the decade leading up to the PDO warm phase (when temperatures are warm in the Gulf of Alaska and cold in the Kuroshio-Oyashio Extension), before switching signs 1.5 years after the PDO maximum. This time evolution is similar but opposite in sign to PDO GMST anomalies (Fig. 3), such that LW anomalies act to damp GMST anomalies. LW anomalies in the decade surrounding a PDO maximum are dominated by positive anomalies (e.g., from more cloud cover) in the central and western equatorial Pacific (135°E-165°W) and negative anomalies (e.g., from less cloud cover) in the Warm Pool, the South Pacific Convergence Zone, and the northeastern subtropical Pacific (Fig. 11b). SW anomalies are opposite in sign in each of these regions (Fig. 11d). The SW anomalies in the North Pacific more closely resemble anomalies in SST than do LW anomalies. These North Pacific SW anomalies suggest a reduction in low cloud cover in regions of positive SST anomalies, as has been observed (Schmeisser et al. 2020). This positive feedback, particularly in the eastern Pacific, has been suggested to play a role in the amplitude and persistence of the PDO (Bellomo et al. 2014).

Positive SW feedbacks dominate the global mean in the period leading up to a PDO warm event (Fig. 11a). In the year following a PDO maximum, negative SW and LW feedbacks reinforce each other, helping to switch the sign of GMST anomalies. SW anomalies remain negative (a positive feedback on negative GMST anomalies) during the decade after a PDO event. The net effect of the SW and LW terms is near zero until a year before a PDO event, followed by net energy loss in the ∼3 year period surrounding a PDO event then net energy gain in the following ∼8 years of negative GMST anomalies (Fig. 11a).

As with other modes of low-frequency variability, the global TOA radiation changes are balanced by changes in ocean heat content. Ocean heat loss during the peak of the PDO event occurs primarily in the Kuroshio current and the central and western equatorial Pacific (135°E-165°W); ocean heat uptake in the following decade primarily occurs in the Oyashio current and the same region of the central and western equatorial Pacific. Averaged over ten years, this amounts to a northward transport of heat from the Kuroshio current into the Oyashio current (Fig. 11c). This anomalous ocean heat transport occurs through an ad-

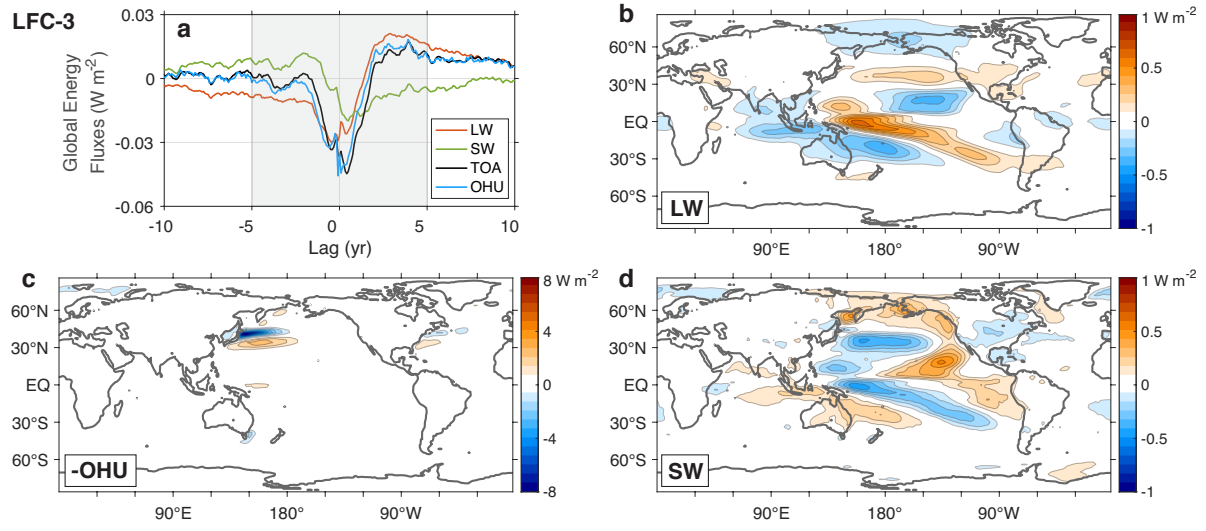

FIG. 11. Decadal-mean impact of the PDO-like LFC-3 on the global energy budget. Panels as described in Fig. 9.

justment of the ocean gyre circulation to changes in wind forcing (Wills et al. 2019b and references therein).

d. El Niño-Southern Oscillation

The global energy budget changes associated with Niño3.4 are opposite in sign between lead times and lag times (Fig. 12a) and largely cancel out in a decadal average centered about lag-0 (Fig. 8a). We therefore focus on global energy budget anomalies separately in the year preceding and the year following an ENSO event, i.e., the build up and decay phase of an ENSO event. Note that our regression approach weights El Niño and La Niña events equally. The lead-lag structure of TOA is similar between El Niño and La Niña events (inset in Fig. 8a), but with the build up phase being weaker and slower and the decay phase being stronger and faster for El Niño events compared to La Niña events.

The lead-lag structure of global TOA radiation (Fig. 12a) is the net result of a longwave component (LW), which evolves in proportion to and acts to damp GMST anomalies (cf. Fig. 3), and a shortwave component (SW), which evolves in quadrature with GMST anomalies (Lutsko and Takahashi 2018). For the months around a peak ENSO event, LW and SW largely cancel, leading to small anomalies in global TOA radiation. At lead or lag times larger than a few months, LW and SW anomalies reinforce each other, leading to large anomalies in global TOA radiation.

At both lead and lag times, LW and SW anomalies are largest in the central and western equatorial Pacific (Fig. 12d,f), where they show the eastward shift of deep convection during El Niño events (Rasmusson and Carpenter 1982; Deser and Wallace 1990). These anomalies largely cancel in the net TOA radiation (Fig. 12b). At lead times, net TOA anomalies are largest in the eastern Pacific (Fig. 12b), where the combined LW and SW feedbacks provide a positive feedback on ENSO growth (Bellomo et al. 2014; Rädel et al. 2016; Middlemas et al. 2019). At lag times, net TOA anomalies are largest in the subtropical Pacific and the Warm Pool (Fig. 12b), where negative LW anomalies (positive OLR anomalies) dominate over positive SW anomalies, resulting in a net loss of energy in regions of weakly positive surface air temperature anomalies (Fig. 12c). These differences in radiative anomalies between lead times and lag times result in a net energy gain leading up to an El Niño event and a net energy loss afterwards. This can result in biases in estimates of climate sensitivity from short records if the averaging period doesn't include the full period of energy gain and loss, as was shown in Section 4.

Temperature and radiation anomalies in the subtropics are larger in the year after a maximum in Niño3.4 than in the year before. Anomalies in these fields therefore cover a broader range of latitudes at lag times, where the temperature pattern resembles the PDO (Zhang et al. 1997). Note, however, that the decadal variability captured by the PDO-like LFC-3 is much more focused in the midlatitudes (Fig. 3) and occurs due to midlatitude processes that are only loosely connected to ENSO (Wills et al. 2019b).

The evolution of ocean heat uptake during and ENSO event looks similar to that of global TOA radiation (Fig. 12a), but with a slight lead such that the total heat content of the ocean is maximum at a lead time of $\sim$3 months and the net heat content of the atmosphere is max-

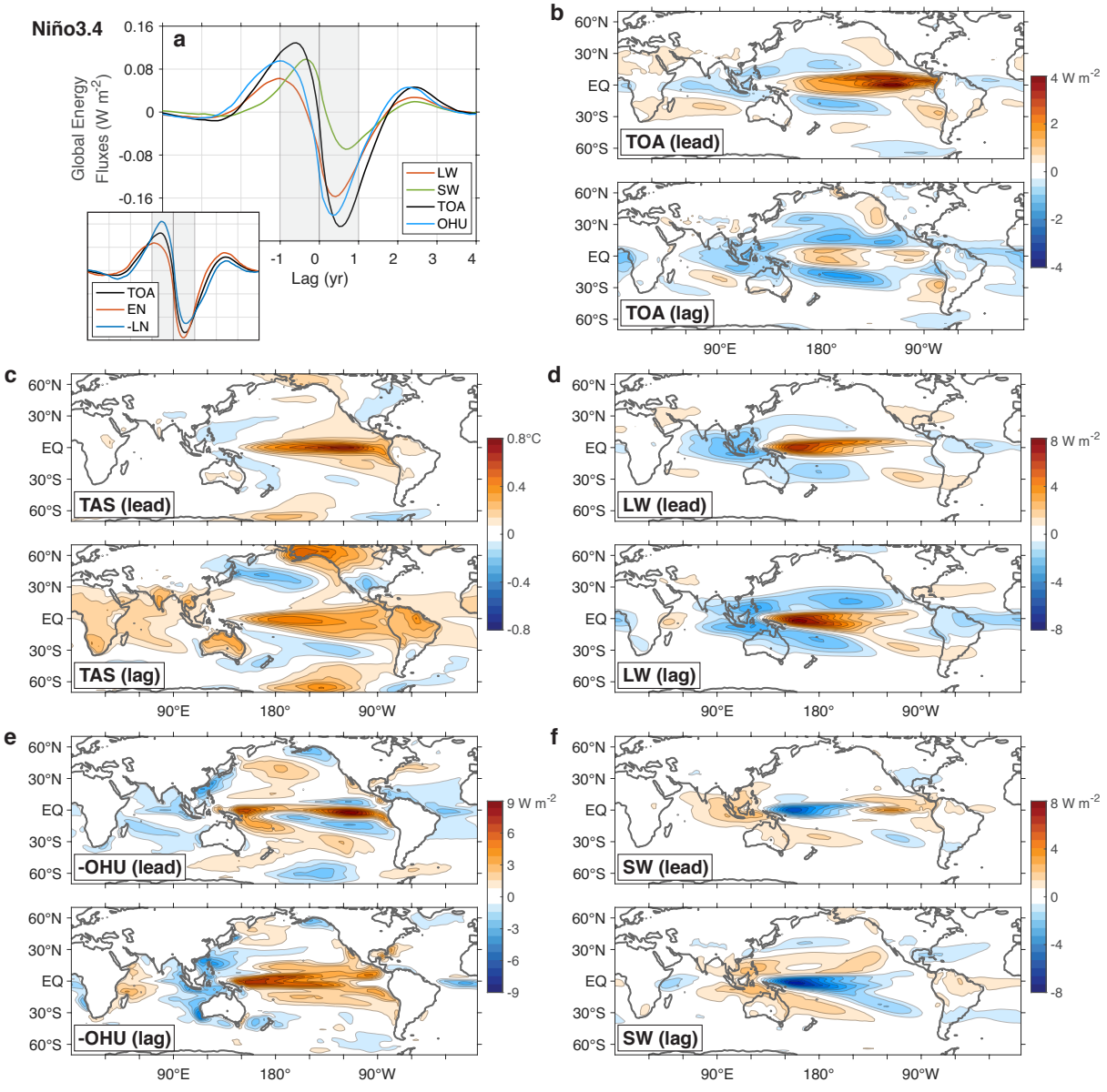

FIG. 12. Impact of ENSO on the global energy budget. (a) Lead-lag regression of net incoming longwave radiation at TOA (LW), net incoming shortwave radiation at TOA (SW), net incoming radiation at TOA, and net ocean heat uptake (OHU) on Niño3.4. Positive TOA flux anomalies correspond to a net energy input to the Earth system. Lag times indicate anomalies that lag Niño3.4. The inset shows the lead-lag regression of TOA separately for El Niño (EN) and La Niña (LN), normalized such that they each have the same variance across all lead and lag times. (b)-(e) Maps of anomalies in (b) net incoming radiation at TOA, (c) surface air temperature (TAS), (d) LW, (e) −OHU, and (e) SW for a 1-standard-deviation anomaly in Niño3.4. Top subpanels show anomalies in the year before the Niño3.4 maximum; bottom subpanels show anomalies in the year after (i.e., 1-yr running mean anomalies at a lead time of 6 months and a lag time of 6 months, respectively). The gray shading in (a) shows the averaging period used in the other subpanels. All calculations are are averaged over 35 CMIP6 models.

imum at a lag time of ∼4 months. The total energy content of the Earth system (as determined by global TOA radiation) peaks just before lag-0, similar to what is found in observational estimates of ocean heat content (Johnson and Birnbaum 2017). Ocean heat uptake at lead times primarily occurs in the Atlantic and Indian Oceans, off the equator in the tropical eastern Pacific, and along the coast of East Asia (Fig. 12e). Along the equator, the ocean is already losing energy in the year before an El Niño event (Fig. 12e), but this energy loss covers a much larger area

in the year following an El Niño event. This heat loss from the ocean surface acts to damp the SST anomalies set up by anomalies in ocean heat transport and upwelling (Zebiak and Cane 1987; Philander 1989; Deser and Wallace 1990). Locally, the net surface heat flux anomalies are larger in magnitude than the anomalies in net TOA radiation (Fig. 12e; cf. Fig. 12b). They are a dominant factor in driving anomalies in tropical overturning circulations such as the Walker circulation, partly through their influence on large-scale SST and sea-level pressure gradients (Chiang et al. 2001; Adames and Wallace 2017) and partly through their direct influence on the strength of ascent in deep convective regions (Wills et al. 2017).

6. Discussion and Conclusions

a. Low-frequency variability in global climate

In this paper, we showed that the CMIP6 models with the largest amplitude of interdecadal GMST variability are dominated by variability in the high-latitude oceans. Interdecadal variability in the Northern Hemisphere (i.e., LFC-1) is closely tied to the AMO/AMV, with large SST anomalies in the North Atlantic subpolar gyre associated with coupled atmosphere-ocean variability (Wills et al. 2019a and references therein). Our analysis indicates some warming of the North Pacific during warm phases of the AMV, but there is not a strong coherence between North Pacific and North Atlantic temperatures, owing in part to decadal variability of the North Pacific that is captured by LFC-3 and LFC-5′. Several modes identified by our analysis similarly show midlatitude SST anomalies in both the Atlantic and Pacific, possibly related to interbasin teleconnections (e.g., Zhang and Delworth 2007). However, such inter-basin relationships should be interpreted with caution, as spatial covariance analyses such as this one are known to show coherent anomalies in regions that are only weakly correlated (Deser 2000).

Interdecadal variability in the Southern Hemisphere is dominated by zonally symmetric SST changes in the Southern Ocean (i.e., LFC-2). In models where this variability is strongest, it is linked to variability in open-ocean deep convection (Martin et al. 2013; Pedro et al. 2016; Behrens et al. 2016; Reintges et al. 2017; Zhang et al. 2017; Cabré et al. 2017). The large area of SST anomalies associated with LFC-1 and LFC-2 as well as their impact on sea-ice extent and Arctic/Antarctic surface air temperatures help them have a large impact on GMST. The long timescale of these modes of variability mean that the associated GMST anomalies can persist for multiple decades (Fig. 3) or even up to a century in some models (Parsons et al. 2020). However, neither of these modes have a large impact on the global energy balance at TOA. In both cases, large, negative longwave radiative feedbacks, which would act to damp GMST anomalies, are cancelled by positive shortwave radiative feedbacks, such as the sea ice-albedo feedback and low-cloud feedback. These cancelling feedbacks result in these modes having weak global radiative feedbacks of approximately -0.5 W m^{-2} K^{-1}. If such low global radiative feedbacks occurred in response to a doubling of CO_2 (something that should only be considered a thought experiment), then this would correspond to an ECS of ~ 8°C.

Cancellation between longwave and shortwave feedbacks also occurs in PDO-like LFC-3 variability, except in the year before and the year after its peak. As a consequence, LFC-3 also has a weak global radiative feedback, though not as weak as LFC-1 and LFC-2. In contrast, longwave and shortwave feedbacks associated with ENSO reinforce each other at most lead and lag times, leading to large impacts on the TOA energy balance. ENSO is therefore the mode of variability with the largest impact on global TOA radiation out to decadal timescales, despite its predominantly interannual timescale. The strong global radiative feedbacks associated with ENSO variability act to damp the associated GMST anomalies and prevent them from persisting for more than a year or two.

We also find that there are a diverse array of possible lead-lag relationships between modes of variability and global climate impacts. While GMST anomalies develop in proportion to LFC-1 and LFC-2 anomalies and (with a few month lag) to ENSO anomalies, this is not the case for the PDO-like LFC-3, which is associated instead with an anomaly in the rate of GMST change. Global TOA radiation anomalies exhibit an even wider range of lead-lag relationships with the modes of variability. In the case of LFC-1 and LFC-2, weakly negative global TOA radiation anomalies develop after their warm phases. However, LFC-2 also shows positive global TOA radiation anomalies in the decades leading up to its warm phase, evidence that positive radiative feedbacks (e.g., the sea ice-albedo feedback) act to amplify its growth. LFC-3 and ENSO radiative anomalies have a similar temporal evolution to their respective GMST anomalies, but with opposite signs and slight lags. In both cases, global TOA radiation anomalies near the peak of the LFC-3 or ENSO event act to change the sign of GMST anomalies. For the case of ENSO, the relationship between global TOA radiation and GMST can be modeled with a stochastically forced linear oscillator (Proistosescu et al. 2018).

Some important caveats of our study are that our analysis was entirely based upon CMIP6 models, that we only considered a subset of the diverse modes of climate variability, and that we made no distinction between anomalies in different seasons. Further work is needed to validate some of our conclusions in observations. In particular, longer records and/or better methods to remove the forced climate response are needed to determine the magnitude of decadal internal variability in observations, especially in the North Atlantic and Southern Ocean. The radiative impacts of these slow modes of high-latitude vari-

ability are also hard to verify in observations until we have longer records of TOA radiation. A more thorough treatment of the seasonality of global energy budget anomalies may also give further insight into the mechanisms of variability in global climate.

b. *Estimating climate sensitivity in the presence of internal variability*

In Section 4, we analyzed the influence of unforced internal variability on estimates of the global climate feedback from short time periods, as have been used to estimate climate sensitivity from observations (Otto et al. 2013; Lewis and Curry 2015; Forster 2016; Knutti et al. 2017; Sherwood et al. 2020). We found that decadal internal variability of the magnitude found in CMIP6 piControl simulations can lead to biases of ± 0.65°C (± 0.36°C) in the effective climate sensitivity (EffCS) inferred from 10-yr (30-yr) average anomalies, when superimposed on externally forced GMST and global energy budget changes of $\overline{T}_{\text{forced}} = 1$°C and $\overline{F} - \overline{N}_{\text{forced}} = 1.14$ W m^{-2}. The spread in EffCS due to internal variability would get larger for smaller forced temperature changes or for smaller global radiative feedbacks (larger effective climate sensitivities).

The biggest contributors to the spread in EffCS are the slow modes of global temperature variability in the high latitudes (LFC-1 and LFC-2), which can each lead to approximately ± 0.2°C biases in EffCS based on decadal averages. Some models suggest that these modes can lead to EffCS spreads up to 5 times as large. ENSO can also lead to biases in EffCS if its lead and lag impacts on the global energy budget are not fully captured by the averaging period; it can lead to an approximately ± 0.15°C bias in EffCS if the averaging period used starts from a 1-standard deviation La Niña event and ends with a 1-standard deviation El Niño event, or vice versa. The PDO-like LFC-3 can lead to anomalies in the rate of GMST change, but does not cause a large impact on decadal-mean EffCS except in models with positive global radiative feedbacks on this GMST change.

Applying these insights on the sources of internal variability in EffCS to estimate the actual EffCS bias in a particular historical period would require further methodological developments (e.g., using detection and attribution methods to track changes in modes of variability over time) that are beyond the scope of this paper. However, we can provide some qualitative arguments for how internal variability influenced recent ECS estimates from observations. During the time periods used by Otto et al. (2013) (2000-2009) and Lewis and Curry (2015) (1995-2011), the high-latitudes of the North Atlantic and Arctic had warmed more than projected in uninitialized climate model simulations (Yeager et al. 2015), while the Southern Ocean had warmed less than projected (Armour et al. 2016). These anomalies correspond to a positive anomaly in LFC-1 and a negative anomaly in LFC-2, though there is still an open question on the extent to which these anomalies resulted purely from internal variability or resulted in part from an externally forced response that is not captured by models. Regardless of their origin, the anomalies in LFC-1 and LFC-2 would lead to large positive and negative EffCS biases, respectively. If these anomalies are due to internal variability, these biases are differences between EffCS and $\text{EffCS}_{\text{forced}}$; if they are due to an incorrect forced response in models, these biases are differences in $\text{EffCS}_{\text{forced}}$ between the real world and models.

There were also large changes in Niño3.4 during these two time periods; the 2000-2009 period started from a moderate La Niña and ended with a moderate El Niño, while the 1995-2011 period started from a weak El Niño and ended with a weak La Niña. Our analysis of the global energy budget impacts of Niño3.4 suggests that these ENSO anomalies at the beginning and end of these time periods could lead to opposite biases in EffCS, with a positive EffCS bias based on 2000-2009 and a negative bias based on 1995-2011. The general agreement between these two estimates, however, suggests that this was not the case. The full time evolution of Niño3.4 during these time periods (rather than just the anomalies at the end points) could be important in determining the anomalies in the global energy budget and the corresponding biases in EffCS. Together, the large global radiative impacts of ENSO and the difficulties in capturing these impacts with a simple linear regression approach suggest that great caution is needed in estimating climate sensitivity from short observational records.

c. *Internal variability as a lens into the forced climate response*

Global radiative feedbacks depend predominantly on the pattern of surface temperature change, regardless of how that temperature change is forced (Haugstad et al. 2017; Dong et al. 2019). Therefore, the radiative response to patterns of internal variability can provide a basis for understanding how the radiative response to anthropogenically forced warming depends on the spatial pattern of warming (Eq. 6). Here, we use our conclusions about internal variability in global climate as a qualitative lens into feedbacks associated with the forced climate response.

The large GMST anomalies and weak global radiative feedback (high effective climate sensitivities) associated with slow modes of internal variability in the high latitudes of the North Atlantic, Southern Ocean, and North Pacific suggests that forced climate change with more warming in these regions (e.g., greater polar amplification) would have a larger climate sensitivity. In contrast, ENSO-like anomalies in CMIP6 models were found to have a small impact on contemporaneous anomalies in effective climate

sensitivity, such that an equilibrium pattern of warming with more or less warming in the eastern equatorial Pacific wouldn't necessarily have a different climate sensitivity. This is consistent with the work of Dong et al. (2019), which shows that it is primarily the relative amount of warming in the western equatorial Pacific, not the eastern equatorial Pacific, that controls the global radiative feedback and climate sensitivity. However, subtle differences in the SST pattern between the build up and decay phases of El Niño can give rise to opposite anomalies in global TOA radiation, larger positive SST anomalies in the Warm Pool during the El Niño decay phase results in stronger net energy loss at TOA. Therefore, ENSO-like forced responses could influence the effective climate sensitivity if their spatial pattern differs even slightly from the SST pattern at peak El Niño, possibly due to coupling between the eastern and western equatorial Pacific.

d. Main takeways

We have shown that modes of interdecadal SST variability in CMIP6 models are concentrated in the high latitudes, where they have a large impact on GMST but a minimal impact on global TOA radiation. The largest and most persistent GMST anomalies result from variability in North Atlantic SSTs linked to AMOC or variability in Southern Ocean SSTs linked to poleward ocean heat transport. The minimal impact of these slow modes of global temperature variability on global TOA radiation results from the cancelation between positive shortwave cloud and sea ice-albedo feedbacks and the negative feedback of outgoing longwave radiation. This is in contrast to modes of tropical SST variability, such as ENSO, which have a large impact on global TOA radiation, but primarily exhibit variability on intradecadal timescales.

We hypothesize that it is not a coincidence that the slowest modes of global temperature variability are in regions of weak radiative feedbacks. Rather, we suggest that the lack of strong radiative damping in the polar regions, where anomalies remain trapped beneath a strong inversion, as well as the relative inefficiency of atmospheric heat transport away from these regions (Stuecker et al. 2018; Armour et al. 2019), may be the reason that SST anomalies in these regions can persist for several decades. In contrast, SST anomalies in regions of tropical deep convection will quickly be communicated to the free troposphere, where they can influence the global lapse rate and cloud fraction and lead to strong radiative damping (Zhou et al. 2017; Ceppi and Gregory 2017; Dong et al. 2019). As a consequence, SST anomalies in tropical deep convective regions would result in a large loss of energy at the global scale. In the absence of a large source of energy (e.g., strong energy exchange with the deep ocean), these tropical SST anomalies would not be able to persist on decadal timescales. We therefore suggest that tropical SST anomalies will always be associated with large changes in Earth's energy budget, whether forced or unforced.

Acknowledgments. R.C.J.W. and D.S.B. acknowledge support from the National Science Foundation (Grant AGS-1929775) and the Tamaki Foundation. R.C.W. and K.C.A. acknowledge support from the National Science Foundation (Grant AGS-1752796). We thank Maria Rugenstein, Jonah Bloch-Johnson, and Aaron Donohoe for valuable input on this work. We thank Peter Huybers for providing scripts for the estimation of spectra and coherence using a multi-taper method, which are available at https://www.people.fas.harvard.edu/~phuybers/Mfiles/. The code for LFCA is available at https://github.com/rcjwills/lfca. We acknowledge the World Climate Research Programme, which, through its Working Group on Coupled Modelling, coordinated and promoted CMIP6. We thank the climate modeling groups for producing and making available their model output, the Earth System Grid Federation (ESGF) for archiving the data and providing access, and the multiple funding agencies who support CMIP6 and ESGF.

APPENDIX A

Contributions to EffCS Spread

Here, we provide expressions for the contributions of internal variability in GMST ($\overline{T}_{\text{internal}}$) and global TOA radiation ($\overline{N}_{\text{internal}}$) to anomalies in EffCS. We start from the full expression for EffCS:

$$\text{EffCS} = -\frac{\overline{F}_{2\text{xCO}_2}(\overline{T}_{\text{forced}} + \overline{T}_{\text{internal}})}{(\overline{R}_{\text{forced}} + \overline{N}_{\text{internal}})}. \tag{A1}$$

For conciseness, we have introduced $\overline{R}_{\text{forced}} = \overline{N}_{\text{forced}} - \overline{F}$. The effective climate sensitivity associated with the forced response is determined by setting $\overline{T}_{\text{internal}}$ and $\overline{N}_{\text{internal}}$ to zero:

$$\text{EffCS}_{\text{forced}} \equiv -\frac{\overline{F}_{2\text{xCO}_2}\overline{T}_{\text{forced}}}{\overline{R}_{\text{forced}}}. \tag{A2}$$

The difference between EffCS and $\text{EffCS}_{\text{forced}}$ is split into 3 components, due to $\overline{T}_{\text{internal}}$, $\overline{N}_{\text{internal}}$, or a combination of the two:

$$\begin{aligned}\text{EffCS}_{\text{GMST}} &\equiv -\frac{\overline{F}_{2\text{xCO}_2}(\overline{T}_{\text{forced}} + \overline{T}_{\text{internal}})}{\overline{R}_{\text{forced}}} - \text{EffCS}_{\text{forced}} \\ &= -\frac{\overline{F}_{2\text{xCO}_2}\overline{T}_{\text{internal}}}{\overline{R}_{\text{forced}}},\end{aligned} \tag{A3}$$

$$\begin{aligned}\text{EffCS}_{\text{TOA}} &\equiv -\frac{\overline{F}_{2\text{xCO}_2}\overline{T}_{\text{forced}}}{(\overline{R}_{\text{forced}} + \overline{N}_{\text{internal}})} - \text{EffCS}_{\text{forced}} \\ &= \frac{\overline{F}_{2\text{xCO}_2}\overline{T}_{\text{forced}}\overline{N}_{\text{internal}}}{\overline{R}_{\text{forced}}(\overline{R}_{\text{forced}} + \overline{N}_{\text{internal}})},\end{aligned} \tag{A4}$$

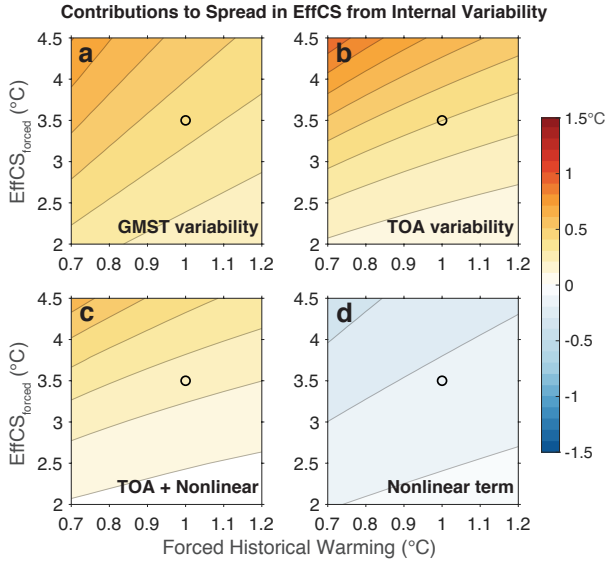

FIG. A1. Contributions to the two-standard-deviation (≈95%) spread in effective climate sensitivity (EffCS), calculated from 10-yr running averages, from internal variability in (a) GMST, (b) global TOA radiation, (c) global TOA radiation and nonlinear terms that depend on the covariance of GMST and global TOA radiation, and (d) the nonlinear terms that depend on the covariance of GMST and global TOA radiation; i.e., (c) = (b) + (d). This calculation is based on the superposition of internal variability from CMIP6 pre-industrial control simulations and an assumed externally forced historical warming ($\overline{T}_{\text{forced}}$, x-axis) and an assumed radiative response corresponding a forced effective climate sensitivity [$\text{EffCS}_{\text{forced}} = \left(\overline{F} - \overline{N}_{\text{forced}}\right)/\overline{T}_{\text{forced}}$, y-axis]. Values are the median across 35 CMIP6 models.

$$\begin{aligned}\text{EffCS}_{\text{nonlinear}} &\equiv \text{EffCS} - \text{EffCS}_{\text{forced}} \\ &\quad - \text{EffCS}_{\text{GMST}} - \text{EffCS}_{\text{TOA}}. \\ &= \frac{\overline{F}_{2\text{xCO}_2}\,\overline{T}_{\text{internal}}\overline{N}_{\text{internal}}}{\overline{R}_{\text{forced}}\left(\overline{R}_{\text{forced}} + \overline{N}_{\text{internal}}\right)}.\end{aligned} \tag{A5}$$

For conciseness, we have omitted several steps of straightforward algebra. The total EffCS spread shown in Fig. 1a is split into these three terms in Figs. A1a, A1b, and A1d, respectively. Fig A1c shows the combination of $\text{EffCS}_{\text{TOA}}$ and $\text{EffCS}_{\text{nonlinear}}$, i.e., all terms that depend on $\overline{N}_{\text{internal}}$. The contribution to the spread in EffCS from $\overline{T}_{\text{internal}}$ (Fig A1a) is larger than the contribution from $\overline{N}_{\text{internal}}$ (including the nonlinear term, Fig A1c) for all values of the forced response; it is much larger in cases where historical global warming is large or $\text{EffCS}_{\text{forced}}$ is small.

References

Adames, Á. F., and J. M. Wallace, 2017: On the tropical atmospheric signature of El Niño. *J. Atmos. Sci.*, **74 (6)**, 1923–1939.

Alexander, M. A., I. Bladé, M. Newman, J. R. Lanzante, N.-C. Lau, and J. D. Scott, 2002: The atmospheric bridge: The influence of ENSO teleconnections on air–sea interaction over the global oceans. *J. Climate*, **15 (16)**, 2205–2231.

Alexander, M. A., C. Deser, and M. S. Timlin, 1999: The reemergence of sst anomalies in the North Pacific Ocean. *J. Climate*, **12 (8)**, 2419–2433.

Andrews, T., J. M. Gregory, and M. J. Webb, 2015: The dependence of radiative forcing and feedback on evolving patterns of surface temperature change in climate models. *Journal of Climate*, **28 (4)**, 1630–1648.

Armour, K. C., C. M. Bitz, and G. H. Roe, 2013: Time-varying climate sensitivity from regional feedbacks. *Journal of Climate*, **26 (13)**, 4518–4534.

Armour, K. C., J. Marshall, J. R. Scott, A. Donohoe, and E. R. Newsom, 2016: Southern Ocean warming delayed by circumpolar upwelling and equatorward transport. *Nature Geoscience*, **9 (7)**, 549–554.

Armour, K. C., N. Siler, A. Donohoe, and G. H. Roe, 2019: Meridional atmospheric heat transport constrained by energetics and mediated by large-scale diffusion. *J. Climate*, **32 (12)**, 3655–3680.

Behrens, E., G. Rickard, O. Morgenstern, T. Martin, A. Osprey, and M. Joshi, 2016: Southern Ocean deep convection in global climate models: A driver for variability of subpolar gyres and Drake Passage transport on decadal timescales. *Journal of Geophysical Research: Oceans*, **121 (6)**, 3905–3925.

Bellomo, K., A. Clement, T. Mauritsen, G. Rädel, and B. Stevens, 2014: Simulating the role of subtropical stratocumulus clouds in driving Pacific climate variability. *J. Climate*, **27 (13)**, 5119–5131.

Bellomo, K., A. C. Clement, L. N. Murphy, L. M. Polvani, and M. A. Cane, 2016: New observational evidence for a positive cloud feedback that amplifies the Atlantic Multidecadal Oscillation. *Geophys. Res. Lett.*, **43 (18)**, 9852–9859.

Bloch-Johnson, J., M. Rugenstein, and D. S. Abbot, 2020: Spatial radiative feedbacks from internal variability using multiple regression. *J. Climate*, **33 (10)**, 4121–4140.

Bond, N., J. Overland, M. Spillane, and P. Stabeno, 2003: Recent shifts in the state of the North Pacific. *Geophys. Res. Lett.*, **30 (23)**.

Broccoli, A. J., K. A. Dahl, and R. J. Stouffer, 2006: Response of the ITCZ to Northern Hemisphere cooling. *Geophysical Research Letters*, **33 (1)**.

Brown, P. T., W. Li, L. Li, and Y. Ming, 2014: Top-of-atmosphere radiative contribution to unforced decadal global temperature variability in climate models. *Geophys. Res. Lett.*, **41 (14)**, 5175–5183.

Brown, P. T., W. Li, and S.-P. Xie, 2015: Regions of significant influence on unforced global mean surface air temperature variability in climate models. *Journal of Geophysical Research: Atmospheres*, **120 (2)**, 480–494.

Brown, P. T., M. S. Lozier, R. Zhang, and W. Li, 2016: The necessity of cloud feedback for a basin-scale Atlantic Multidecadal Oscillation. *Geophys. Res. Lett.*, **43 (8)**, 3955–3963.

Cabré, A., I. Marinov, and A. Gnanadesikan, 2017: Global atmospheric teleconnections and multidecadal climate oscillations driven by Southern Ocean convection. *Journal of Climate*, **30 (20)**, 8107–8126.

Capotondi, A., and Coauthors, 2015: Understanding ENSO diversity. *Bulletin of the American Meteorological Society*, **96 (6)**, 921–938.

Ceppi, P., and J. M. Gregory, 2017: Relationship of tropospheric stability to climate sensitivity and Earth's observed radiation budget.

Proceedings of the National Academy of Sciences, **114 (50)**, 13 126–13 131.

Charney, J. G., and Coauthors, 1979: *Carbon dioxide and climate: a scientific assessment*. National Academy of Sciences, Washington, DC.

Chen, X., and K.-K. Tung, 2014: Varying planetary heat sink led to global-warming slowdown and acceleration. *Science*, **345 (6199)**, 897–903.

Chen, X., and K.-K. Tung, 2017: Global-mean surface temperature variability: space–time perspective from rotated EOFs. *Climate Dynamics*, 1–14.

Chen, X., and J. M. Wallace, 2016: Orthogonal PDO and ENSO indices. *Journal of Climate*, **29 (10)**, 3883–3892.

Chiang, J. C., and C. M. Bitz, 2005: Influence of high latitude ice cover on the marine Intertropical Convergence Zone. *Climate Dynamics*, **25 (5)**, 477–496.

Chiang, J. C., and D. J. Vimont, 2004: Analogous Pacific and Atlantic meridional modes of tropical atmosphere–ocean variability. *J. Climate*, **17 (21)**, 4143–4158.

Chiang, J. C., S. E. Zebiak, and M. A. Cane, 2001: Relative roles of elevated heating and surface temperature gradients in driving anomalous surface winds over tropical oceans. *J. Atmos. Sci.*, **58 (11)**, 1371–1394.

DelSole, T., 2001: Optimally persistent patterns in time-varying fields. *J. Atmos. Sci.*, **58 (11)**, 1341–1356.

DelSole, T., M. K. Tippett, and J. Shukla, 2011: A significant component of unforced multidecadal variability in the recent acceleration of global warming. *Journal of Climate*, **24 (3)**, 909–926.

Déqué, M., 1988: 10-day predictability of the Northern Hemisphere winter 500-mb height by the ECMWF operational model. *Tellus A*, **40 (1)**, 26–36.

Deser, C., 2000: On the teleconnectivity of the "Arctic Oscillation". *Geophys. Res. Lett.*, **27 (6)**, 779–782.

Deser, C., and J. M. Wallace, 1990: Large-scale atmospheric circulation features of warm and cold episodes in the tropical Pacific. *Journal of Climate*, **3 (11)**, 1254–1281.

Dessler, A., 2013: Observations of climate feedbacks over 2000–10 and comparisons to climate models. *J. Climate*, **26 (1)**, 333–342.

Dessler, A. E., T. Mauritsen, and B. Stevens, 2018: The influence of internal variability on Earth's energy balance framework and implications for estimating climate sensitivity. *Atmospheric Chemistry and Physics*, **18 (7)**.

DiLorenzo, E., and Coauthors, 2008: North Pacific Gyre Oscillation links ocean climate and ecosystem change. *Geophys. Res. Lett.*, **35 (8)**.

Dong, Y., C. Proistosescu, K. C. Armour, and D. S. Battisti, 2019: Attributing historical and future evolution of radiative feedbacks to regional warming patterns using a Green's function approach: The preeminence of the Western Pacific. *J. Climate*, **32 (17)**, 5471–5491.

England, M. H., and Coauthors, 2014: Recent intensification of wind-driven circulation in the Pacific and the ongoing warming hiatus. *Nature Climate Change*, **4 (3)**, 222.

Eyring, V., S. Bony, G. A. Meehl, C. A. Senior, B. Stevens, R. J. Stouffer, and K. E. Taylor, 2016: Overview of the Coupled Model Intercomparison Project Phase 6 (CMIP6) experimental design and organization. *Geoscientific Model Development*, **9 (5)**, 1937–1958.

Forster, P. M., 2016: Inference of climate sensitivity from analysis of Earth's energy budget. *Annual Review of Earth and Planetary Sciences*, **44**, 85–106.

Frankcombe, L. M., M. H. England, M. E. Mann, and B. A. Steinman, 2015: Separating internal variability from the externally forced climate response. *Journal of Climate*, **28 (20)**, 8184–8202.

Gregory, J., and Coauthors, 2004: A new method for diagnosing radiative forcing and climate sensitivity. *Geophys. Res. Lett.*, **31 (3)**.

Haugstad, A., K. Armour, D. Battisti, and B. Rose, 2017: Relative roles of surface temperature and climate forcing patterns in the inconstancy of radiative feedbacks. *Geophysical Research Letters*, **44 (14)**, 7455–7463.

Johnson, G. C., and A. N. Birnbaum, 2017: As El Niño builds, Pacific Warm Pool expands, ocean gains more heat. *Geophys. Res. Lett.*, **44 (1)**, 438–445.

Jones, P. D., 1989: The influence of ENSO on global temperatures. *Climate Monitor*, **17**, 80–89.

Kaiser, H. F., 1958: The varimax criterion for analytic rotation in factor analysis. *Psychometrika*, **23 (3)**, 187–200.

Keenlyside, N., M. Latif, J. Jungclaus, L. Kornblueh, and E. Roeckner, 2008: Advancing decadal-scale climate prediction in the North Atlantic sector. *Nature*, **453 (7191)**, 84.

Knutti, R., M. A. Rugenstein, and G. C. Hegerl, 2017: Beyond equilibrium climate sensitivity. *Nature Geoscience*, **10 (10)**, 727–736.

Kosaka, Y., and S.-P. Xie, 2013: Recent global-warming hiatus tied to equatorial Pacific surface cooling. *Nature*, **501 (7467)**, 403.

Latif, M., T. Martin, and W. Park, 2013: Southern Ocean sector centennial climate variability and recent decadal trends. *Journal of Climate*, **26 (19)**, 7767–7782.

Lewis, N., and J. A. Curry, 2015: The implications for climate sensitivity of AR5 forcing and heat uptake estimates. *Climate Dynamics*, **45 (3-4)**, 1009–1023.

Li, Z., W. Zhang, F.-F. Jin, M. F. Stuecker, C. Sun, A. F. Levine, H. Xu, and C. Liu, 2020: A robust relationship between multidecadal global warming rate variations and the Atlantic multidecadal variability. *Climate Dynamics*, 1–15.

Liu, W., S.-P. Xie, and J. Lu, 2016: Tracking ocean heat uptake during the surface warming hiatus. *Nature communications*, **7**, 10 926.

Loeb, N. G., W. Su, and S. Kato, 2016: Understanding climate feedbacks and sensitivity using observations of earth's energy budget. *Current Climate Change Reports*, **2 (4)**, 170–178.

Lutsko, N. J., and K. Takahashi, 2018: What can the internal variability of CMIP5 models tell us about their climate sensitivity? *Journal of Climate*, **31 (13)**, 5051–5069.

Mahajan, S., R. Zhang, and T. L. Delworth, 2011: Impact of the Atlantic meridional overturning circulation (AMOC) on Arctic surface air temperature and sea ice variability. *J. Climate*, **24 (24)**, 6573–6581.

Mantua, N. J., S. R. Hare, Y. Zhang, J. M. Wallace, and R. C. Francis, 1997: A Pacific interdecadal climate oscillation with impacts on salmon production. *Bulletin of the American Meteorological Society*, **78 (6)**, 1069–1080.

Martin, T., W. Park, and M. Latif, 2013: Multi-centennial variability controlled by Southern Ocean convection in the Kiel Climate Model. *Climate Dynamics*, **40 (7-8)**, 2005–2022.

Meehl, G. A., J. M. Arblaster, J. T. Fasullo, A. Hu, and K. E. Trenberth, 2011: Model-based evidence of deep-ocean heat uptake during surface-temperature hiatus periods. *Nature Climate Change*, **1 (7)**, 360.

Meehl, G. A., A. Hu, J. M. Arblaster, J. Fasullo, and K. E. Trenberth, 2013: Externally forced and internally generated decadal climate variability associated with the Interdecadal Pacific Oscillation. *Journal of Climate*, **26 (18)**, 7298–7310.

Menary, M. B., D. L. Hodson, J. I. Robson, R. T. Sutton, and R. A. Wood, 2015: A mechanism of internal decadal Atlantic Ocean variability in a high-resolution coupled climate model. *J. Climate*, **28 (19)**, 7764–7785.

Middlemas, E. A., and A. C. Clement, 2016: Spatial patterns and frequency of unforced decadal-scale changes in global mean surface temperature in climate models. *J. Climate*, **29 (17)**, 6245–6257.

Middlemas, E. A., A. C. Clement, B. Medeiros, and B. Kirtman, 2019: Cloud radiative feedbacks and El Niño–Southern Oscillation. *J. Climate*, **32 (15)**, 4661–4680.

Muller, R. A., and Coauthors, 2013: Decadal variations in the global atmospheric land temperatures. *Journal of Geophysical Research: Atmospheres*, **118 (11)**, 5280–5286.

Newman, M., and Coauthors, 2016: The Pacific Decadal Oscillation, revisited. *Journal of Climate*, **29 (12)**, 4399–4427.

Olonscheck, D., M. Rugenstein, and J. Marotzke, 2020: Broad consistency between observed and simulated trends in sea surface temperature patterns. *Geophys. Res. Lett.*, e2019GL086773.

Otto, A., and Coauthors, 2013: Energy budget constraints on climate response. *Nature Geoscience*, **6 (6)**, 415.

Palmer, M. D., D. J. McNeall, and N. J. Dunstone, 2011: Importance of the deep ocean for estimating decadal changes in Earth's radiation balance. *Geophys. Res. Lett.*, **38 (13)**.

Parsons, L., and G. Hakim, 2019: Local regions associated with interdecadal global temperature variability in the Last Millennium Reanalysis and CMIP5 models. *Journal of Geophysical Research: Atmospheres*, **124 (17-18)**, 9905–9917.

Parsons, L. A., M. K. Brennan, R. C. Wills, and C. Proistosescu, 2020: Magnitudes and spatial patterns of interdecadal temperature variability in CMIP6. *Geophys. Res. Lett.*, **47 (7)**, e2019GL086 588.

Pedro, J. B., T. Martin, E. J. Steig, M. Jochum, W. Park, and S. O. Rasmussen, 2016: Southern ocean deep convection as a driver of Antarctic warming events. *Geophys. Res. Lett.*, **43 (5)**, 2192–2199.

Philander, S. G., 1989: El Niño, La Niña, and the Southern Oscillation. *International Geophysics Series*, **46**, 293.

Proistosescu, C., A. Donohoe, K. C. Armour, G. H. Roe, M. F. Stuecker, and C. M. Bitz, 2018: Radiative feedbacks from stochastic variability in surface temperature and radiative imbalance. *Geophysical Research Letters*, **45 (10)**, 5082–5094.

Rädel, G., T. Mauritsen, B. Stevens, D. Dommenget, D. Matei, K. Bellomo, and A. Clement, 2016: Amplification of El Niño by cloud longwave coupling to atmospheric circulation. *Nature Geoscience*, **9 (2)**, 106–110.

Rasmusson, E. M., and T. H. Carpenter, 1982: Variations in tropical sea surface temperature and surface wind fields associated with the Southern Oscillation/El Niño. *Monthly Weather Review*, **110 (5)**, 354–384.

Reintges, A., T. Martin, M. Latif, and W. Park, 2017: Physical controls of Southern Ocean deep-convection variability in CMIP5 models and the Kiel Climate Model. *Geophys. Res. Lett.*, **44 (13)**, 6951–6958.

Risbey, J. S., S. Lewandowsky, C. Langlais, D. P. Monselesan, T. J. O'Kane, and N. Oreskes, 2014: Well-estimated global surface warming in climate projections selected for ENSO phase. *Nature Climate Change*, **4 (9)**, 835.

Schmeisser, L., T. Ackerman, and N. Bond, 2020: Marine heatwaves confirm cloud response to warming in global climate models. *AGU Advances, submitted*, doi:10.1002/essoar.10503088.1.

Schneider, T., and S. M. Griffies, 1999: A conceptual framework for predictability studies. *J. Climate*, **12 (10)**, 3133–3155.

Schneider, T., and I. M. Held, 2001: Discriminants of twentieth-century changes in earth surface temperatures. *J. Climate*, **14 (3)**, 249–254.

Sherwood, S., and Coauthors, 2020: An assessment of Earth's climate sensitivity using multiple lines of evidence. *Reviews of Geophysics*, **58 (4)**, e2019RG000 678.

Stolpe, M. B., I. Medhaug, and R. Knutti, 2017: Contribution of Atlantic and Pacific multidecadal variability to twentieth-century temperature changes. *Journal of Climate*, **30 (16)**, 6279–6295.

Stolpe, M. B., I. Medhaug, J. Sedláček, and R. Knutti, 2018: Multidecadal variability in global surface temperatures related to the Atlantic Meridional Overturning Circulation. *Journal of Climate*, **31 (7)**, 2889–2906.

Stuecker, M. F., and Coauthors, 2018: Polar amplification dominated by local forcing and feedbacks. *Nature Climate Change*, **8 (12)**, 1076–1081.

Takahashi, K., A. Montecinos, K. Goubanova, and B. Dewitte, 2011: ENSO regimes: Reinterpreting the canonical and Modoki El Niño. *Geophys. Res. Lett.*, **38 (10)**.

Timmermann, A., and Coauthors, 2018: El Niño–Southern Oscillation complexity. *Nature*, **559 (7715)**, 535–545.

Ting, M., Y. Kushnir, R. Seager, and C. Li, 2009: Forced and internal twentieth-century SST trends in the North Atlantic. *J. Climate*, **22 (6)**, 1469–1481.

Trenberth, K. E., J. M. Caron, D. P. Stepaniak, and S. Worley, 2002: Evolution of El Niño–Southern Oscillation and global atmospheric surface temperatures. *Journal of Geophysical Research: Atmospheres*, **107 (D8)**, AAC–5.

Trenberth, K. E., and J. T. Fasullo, 2013: An apparent hiatus in global warming? *Earth's Future*, **1 (1)**, 19–32.

Tung, K.-K., X. Chen, J. Zhou, and K.-F. Li, 2018: Interdecadal variability in pan-Pacific and global SST, revisited. *Climate Dynamics*, 1–13.

Venzke, S., M. R. Allen, R. T. Sutton, and D. P. Rowell, 1999: The atmospheric response over the North Atlantic to decadal changes in sea surface temperature. *J. Climate*, **12 (8)**, 2562–2584.

Watanabe, M., J.-L. Dufresne, Y. Kosaka, T. Mauritsen, and H. Tatebe, 2020: Enhanced warming constrained by past trends in equatorial Pacific sea surface temperature gradient. *Nature Climate Change*, 1–5.

Wigley, T., 2000: ENSO, volcanoes and record-breaking temperatures. *Geophys. Res. Lett.*, **27 (24)**, 4101–4104.

Wills, R. C., X. J. Levine, and T. Schneider, 2017: Local energetic constraints on Walker circulation strength. *Journal of the Atmospheric Sciences*, **74 (6)**, 1907–1922.

Wills, R. C., T. Schneider, J. M. Wallace, D. S. Battisti, and D. L. Hartmann, 2018: Disentangling global warming, multidecadal variability, and El Niño in Pacific temperatures. *Geophys. Res. Lett.*, **45 (5)**, 2487–2496.

Wills, R. C. J., K. C. Armour, D. S. Battisti, and D. L. Hartmann, 2019a: Ocean-atmosphere dynamic coupling fundamental to the Atlantic Multidecadal Oscillation. *J. Climate*, **32 (1)**, 251–272.

Wills, R. C. J., D. S. Battisti, K. C. Armour, T. Schneider, and C. Deser, 2020: Pattern recognition methods to separate forced responses from internal variability in climate model ensembles and observations. *J. Climate*, **33 (20)**, 8693–8719.

Wills, R. C. J., D. S. Battisti, C. Proistosescu, L. Thompson, D. L. Hartmann, and K. C. Armour, 2019b: Ocean circulation signatures of North Pacific decadal variability. *Geophys. Res. Lett.*, **46 (3)**, 1690–1701.

Xie, S.-P., Y. Kosaka, and Y. M. Okumura, 2016: Distinct energy budgets for anthropogenic and natural changes during global warming hiatus. *Nature Geoscience*, **9 (1)**, 29–33.

Yeager, S. G., A. R. Karspeck, and G. Danabasoglu, 2015: Predicted slowdown in the rate of Atlantic sea ice loss. *Geophys. Res. Lett.*, **42 (24)**, 10–704.

Yuan, T., L. Oreopoulos, M. Zelinka, H. Yu, J. R. Norris, M. Chin, S. Platnick, and K. Meyer, 2016: Positive low cloud and dust feedbacks amplify tropical North Atlantic multidecadal oscillation. *Geophys. Res. Lett.*, **43 (3)**, 1349–1356.

Zebiak, S. E., and M. A. Cane, 1987: A model El Niñ–Southern Oscillation. *Monthly Weather Review*, **115 (10)**, 2262–2278.

Zhang, L., T. L. Delworth, and L. Jia, 2017: Diagnosis of decadal predictability of Southern Ocean sea surface temperature in the GFDL CM2.1 model. *J. Climate*, **30 (16)**, 6309–6328.

Zhang, R., and T. L. Delworth, 2007: Impact of the Atlantic multidecadal oscillation on North Pacific climate variability. *Geophys. Res. Lett.*, **34 (23)**.

Zhang, R., T. L. Delworth, and I. M. Held, 2007: Can the Atlantic Ocean drive the observed multidecadal variability in Northern Hemisphere mean temperature? *Geophys. Res. Lett.*, **34 (2)**.

Zhang, Y., J. M. Wallace, and D. S. Battisti, 1997: ENSO-like interdecadal variability: 1900–93. *J. Climate*, **10 (5)**, 1004–1020.

Zhou, C., M. D. Zelinka, and S. A. Klein, 2017: Analyzing the dependence of global cloud feedback on the spatial pattern of sea surface temperature change with a Green's function approach. *Journal of Advances in Modeling Earth Systems*, **9 (5)**, 2174–2189.